

# Quantitative imaging of concentrated suspensions under flow

Lucio Isa, Rut Besseling, Andrew B Schofield, and Wilson C K Poon  
*Scottish Universities Physics Alliance (SUPA) and The School of Physics and Astronomy,  
The University of Edinburgh,  
Kings Buildings, Mayfield Road,  
Edinburgh EH9 3JZ, United Kingdom.*

(Dated: February 3, 2022)

We review recent advances in imaging the flow of concentrated suspensions, focussing on the use of confocal microscopy to obtain time-resolved information on the single-particle level in these systems. After motivating the need for quantitative (confocal) imaging in suspension rheology, we briefly describe the particles, sample environments, microscopy tools and analysis algorithms needed to perform this kind of experiments. The second part of the review focusses on microscopic aspects of the flow of concentrated model hard-sphere-like suspensions, and the relation to non-linear rheological phenomena such as yielding, shear localization, wall slip and shear-induced ordering. Both Brownian and non-Brownian systems will be described. We show how quantitative imaging can improve our understanding of the connection between microscopic dynamics and bulk flow.

PACS numbers: 83.80.Hj, 83.50.Ha, 83.60.La, 61.20.Ne, 61.43.Fs, 82.70.Dd

## Contents

<b>I. Introduction</b>	1
<b>II. Experimental Methods</b>	3
A. The colloidal particles	3
B. Imaging	5
1. Confocal microscopy	6
C. Flow geometries	6
1. Parallel plate shear cells	7
2. Rotational geometries	7
3. Capillaries and micro-channels	8
<b>III. Image analysis</b>	9
A. General methods	9
B. Locating particles	9
C. Tracking algorithms	10
1. Conventional Tracking	11
2. Correlated Image Tracking	11
<b>IV. Imaging of systems under deformation and flow</b>	11
A. Disordered systems	11
1. Slow glassy flows	11
2. Fast channel flow of fluids and pastes	14
3. Non-Brownian suspensions	15
B. Ordered systems and ordering under flow	16
1. Hard-sphere colloids	16
2. Non-Brownian suspensions	18
<b>V. Conclusion and outlook</b>	18
<b>VI. Acknowledgements</b>	19
<b>References</b>	19

## I. INTRODUCTION

Understanding the deformation and flow, or rheology, of complex fluids in terms of their constituents (colloids, polymers, or surfactants) poses deep fundamental challenges, and has wide applications [1]. Compared to the level of understanding now available for the rheology of polymer melts, the rheology of concentrated suspensions lags considerably behind. In the case of polymer melts, it is now possible to predict with some confidence flow fields in complex geometries starting from a knowledge of molecular properties [2]. No corresponding fundamental understanding is yet available for concentrated colloids. The reasons for this are as follows [3], Figure 1.

In a polymer melt, each chain moves under the topological constraints imposed by many other chains. The number of these constraints, typically of order  $10^3$ , is sufficiently large that a mean field picture, the so-called tube model, can be successfully applied [1]. Moreover, the topological entanglement between chains means that the breaking of covalent bonds is needed to impose large deformations, so that strains often remain small ( $\ll 1$ ). In contrast, the maximum number of neighbours in a (monodisperse) suspension of spheres is about 10, so that mean-field averaging of nearest-neighbour cages will not work, and local processes showing large spatio-temporal heterogeneities are expected to be important. Moreover, no topological constraints prevent the occurrence of strains of order unity or higher, so that very large deformations are routinely encountered. These two characteristics alone render suspension rheology much more difficult. Added on top of these difficulties is the fact that concentrated suspensions are in general non-ergodic, i.e. they are stuck in some solid-like, non-equilibrium amorphous state. On the other hand, in a monodisperse system or in a mixture with carefully chosen size ratios, highly-ordered (crystalline) states can occur. In either

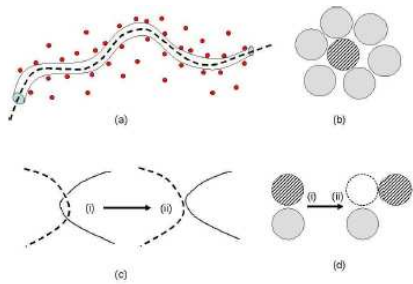


FIG. 1: A schematic comparison between polymer melt rheology and colloid rheology. (a) In a polymer melt, a typical chain (dashed curve) is constrained by many (in reality,  $\sim 10^3$ ) other chains, here represented by small circles. This gives rise to the fruitful mean-field concept of a tube in which the chain has to move. (b) In a concentrated colloidal suspension, a typical particle (hatched) is surrounded (in 3D) by  $\sim 10$  neighbours. This number is too small for mean-field averaging to be meaningful. (c) Large deformations in polymer melts, such as the process (i)  $\rightarrow$  (ii), involves breaking covalent bonds, and so do not ordinarily occur. (d) There are no covalent constraints on order unity deformations, such as (i)  $\rightarrow$  (ii), in a colloidal suspension.

case, any flow necessarily entails non-linearity (yielding, etc.). Moreover, a suspension is a multiphase system, so that the relative flow of particles and solvent can, and often does, become important. This complication does not arise in polymer melts. Finally, compared to the considerable effort devoted to the synthesis and experimental study of very well characterized model materials in polymer melts, corresponding work in colloid rheology remains relatively rare. It is therefore not surprising that the rheology of concentrated suspensions is not nearly as well understood as that of polymer melts.

Advances in this field will pay rich dividends - the successful processing and application of concentrated colloids more often than not depends on understanding, tuning and exploiting their unique flow properties [4]. But to build and validate predictive theories of bulk rheological properties, we need microstructural information. A case study of this claim comes from recent work on the qualitatively distinct rheologies of so-called repulsive and attractive colloidal glasses.

Colloidal glasses are concentrated suspensions in which long-range diffusion effectively vanishes [5]. These dynamically-arrested amorphous states have finite shear moduli in the low-frequency limit. In slightly polydisperse hard-sphere like suspensions, the transition from an ergodic fluid (where long-range diffusion is possible) to a glass occurs at a particle volume fraction of  $\phi \approx 0.58$  [6, 7]. The cause of dynamical arrest is crowding. As  $\phi$  increases, each particle spends longer and longer being caged by its nearest neighbours, until at  $\phi \approx 0.58$ , the life time of these cages becomes longer than any reasonable experimental time window. Each particle can still undergo Brownian motion within its nearest-neighbour cage, but its root mean-square displacement saturates at

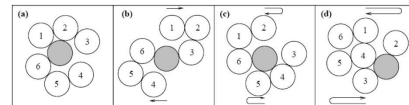


FIG. 2: Cartoon of two different yielding mechanisms in an attractive glass under oscillatory shear (motion indicated by arrows). (a) Un-sheared configuration of particles at time zero. The shaded particles bonding neighbours are particles 1, 2 and 6 and topological neighbours are particles 1-6. At small shear amplitude  $\gamma_0$  the particles retain the same topology during shear. (b) Above the lower yield strain, bonds break. (c) After one period of oscillatory shear, the shaded particle retains the same topological neighbours but different bonding neighbours, cf. (a). (d) If the strain amplitude exceeds the higher yield strain, the identity of the topological neighbours around the shaded particle is changed after one period of shear, cf. (a), the glass is melted and becomes liquid-like.

just over  $0.1a$  (where  $a$  is the particle radius) [7], this quantity being a measure of the time-averaged fluctuating cage size. When oscillatory shear strain is applied to a hard-sphere colloidal glass, yielding occurs in a single-step process at a strain amplitude of just over 10% [8]. This has been interpreted in terms of cage breaking; the glass yields when nearest-neighbour cages are strained beyond their natural (thermally induced) deformation.

When a strong enough short-range attraction is present (where short means a few per cent of  $a$ , a second type of glassy state occurs - the attractive glass, in which arrest is due to particles being trapped by nearest neighbour bonds [9]. It turns out that under oscillatory strain, an attractive glass yields in a two-stepped process [10]. The first step occurs at a strain amplitude of a few per cent, matching the range of the interparticle attraction, and then at a second step when the strain amplitude reaches a few tens of per cent. The first step has been interpreted as the breaking of interparticle bonds, Figure 2. Once these are broken many times, however, each particle realises that it is still in a topological cage formed by its neighbours. A second, cage breaking, step is still necessary for complete yielding to occur. This two step signature is discernible in other rheological tests applied to attractive colloidal glasses [11].

For the purposes of this review, the important point is that the explanation proposed for the observed qualitative difference between repulsive and attractive glass rheology have been couched in microstructural terms, Figure 2. Thus, conclusive validation of these explanations depends on studying yielding at the single-particle level. Such investigation can, in principle, be performed using computer simulations. But simulating particles under flow with realistic system sizes and including hydrodynamic interactions is a major challenge, although progress is being made (see the useful introduction in [12] and references therein). Experimentally, the situation is also difficult. Until comparatively recently, the method of choice for obtaining microstructural information in col-

loids is scattering (X ray, neutron or light), whether in quiescent or flowing systems. But scattering can provide information on the average structure; obtaining local information is difficult, if not impossible. The ideal method for gaining local information is direct imaging.

The appropriate imaging method of imaging colloids depends, of course, on a number of factors, principally perhaps the size and concentration of the particles concerned. The size imposes a basic constraint, so that, for example, visible light can only be used to image particles (at least in the ‘far field’) with radius  $\gtrsim 300$  nm. The concentration is also an important factor, because any multiple scattering by concentrated systems will degrade image quality. In this review, we focus on the use of *confocal* optical microscopy to study colloidal systems under flow. Confocal imaging rejects out-of-focus information using suitably placed pinholes, thus permitting the study of concentrated systems. While the use of confocal microscopy to study quiescent concentrated colloids is, by now, well established [13, 14, 15, 16], the extension to flow is relatively recent. The quantitative use of this methodology depends on developments in both hardware and software. First, to minimise image distortion, *fast* confocal scanning is necessary; we review recent developments in this area in Section II B 1. Moreover, sample geometries are required for simultaneous flow/rheometry and imaging, which we review in Section II C. In terms of software, algorithms must be developed to track particles from image sequences distorted by flow; such algorithms are explained in Section III. After discussing these methodological issues, we turn to review a number of applications (Section IV).

To date, the use of quantitative confocal microscopy to image concentrated colloids under flow has been applied mostly to the study of very well characterised, model systems, particularly systems of particles that interact as more or less perfect hard spheres. The focus on model systems is partly dictated by the desire to obtain as high quality images as possible, which requires the matching of the refractive indices of the particles and the suspending medium (see Section II A). The degree of control necessary, both in the particle synthesis and in solvent choice, is only really achievable in model systems. The reason for choosing to study hard spheres is that these represent the simplest possible (classical) strongly-interacting particles. The properties of a quiescent collection of hard spheres are well understood in statistical mechanical terms, much of this understanding having been obtained in the last few decades through the study of model hard-sphere colloids. It is therefore natural to extend such studies into the area of *driven* systems.

We first briefly summarize the quiescent behaviour of ideal hard spheres. As first shown via numerical simulations [17, 18], below a volume fraction of  $\phi_F = 0.494$ , the thermodynamically stable phase is a fluid of colloidal particles. Long-ranged order is absent and the particles are able to explore all available space (the system is ergodic). For  $0.494 < \phi < 0.545$ , the equilibrium state

is a coexistence of a fluid phase and a crystalline phase. At  $\phi_C = 0.545$  the entire system must be crystalline to minimise the free energy, and this remains the case up to the (crystalline) closed packing fraction of  $\phi_{CP} = 0.74$ . This behaviour was largely confirmed by the experiments of Pusey and van Meegen [6] using sterically-stabilised PMMA particles (for which see the next section). But, they also found that their system failed to crystallize for volume fractions  $\phi \gtrsim \phi_G = 0.58$ , remaining ‘stuck’ in a non-ergodic (or glassy) state up to the maximum possible concentration for amorphous packing (which, for monodisperse hard spheres, is  $\phi_{RCP} \simeq 0.64$ ). We have already introduced such colloidal glasses. Our review of microscopic phenomena will cover both the flow of amorphous states (Section IV A) and of ordered (or ordering) states (Section IV B) of concentrated colloids. While our focus will be on hard-sphere colloids, we will also mention various imaging studies on the the flow of non-Brownian suspensions.

## II. EXPERIMENTAL METHODS

### A. The colloidal particles

One of the key ingredients for high-quality confocal imaging of concentrated suspensions is a colloidal system that allows identification of the individual spheres, does not suffer from rapid photobleaching and gives good depth penetration into the bulk of the dispersion. Fluorescently-labelled poly-methyl-methacrylate (PMMA) particles in hydrocarbon solvents show these characteristics.

The synthesis of hard-sphere PMMA particles was first described by Barrett [19] in 1975 and subsequently by Antl *et al.* [20] in 1986. It is a two-stepped dispersion polymerization reaction, yielding particles made of PMMA cores kept stable by a thin ( $\simeq 10$ nm) outer layer of poly-12-hydroxystearic acid chains, which act as a steric barrier to aggregation. In the first step of the polymerization the spheres are made by growing PMMA chains in solution, which become insoluble when they reach a certain size. At this point they come out of solution and clump together to form particles that are kept stable by physisorbed poly-12-hydroxystearic acid chains. The second step of the preparation involves chemically linking the stabiliser chains to the spheres. These chains are tightly packed on the particle surface [21] and stretch out in good solvents such as various hydrocarbons, which causes the particles to interact as nearly-perfect hard-spheres [22]. The resulting particles can have polydispersities as low as a few percent, and can be made with radii ranging from 100 nm up to and above 1  $\mu$ m.

Fluorescent labelling of the particles for confocal microscopy may be achieved in three ways. The first involves the use of polymerisable dyes. These dyes have been chemically modified to include a reactive group that can be chemically attached to the particle as they

are produced. The advantage of this procedure is that the dye will not leave the particle once it is incorporated. For sterically-stabilised PMMA particles this involves adding a methacrylate group to the dye, and several such procedures [23, 24, 25, 26, 27] have been described in the literature. The most commonly used dye is 7-nitrobenzo-2-oxa-1,3-diazole-methyl methacrylate (NBD-MMA) [26, 27], which is excited at 488nm and emits at 525nm, while the red end of the spectrum is well served by (rhodamine isothiocyanate)-aminostyrene (RAS) [27].

The second way to dye the PMMA spheres is to add an unreactive species during particle formation. Here the dye has no polymerisable group and is just dissolved in one of the reaction reagents with the hope that it will become incorporated into the growing particle. The advantage of this method is that no chemistry, which may alter the dye's physical properties, is required prior to use; it also allows for a wider range of dyes. The disadvantage is that the dye may leak out when, for example, solvency conditions are changed, or migrate within the particle. This technique was employed by Campbell and Bartlett [28], who examined how four different red dyes affected particle formation. They found optimum properties when using 1,1-dioctadecyl-3,3,3,3-tetramethylindocarbocyanine (DiIC18), which had significantly slower photobleaching rate than other dyes tested, did not affect particle preparation and did not interfere with the hard-sphere behaviour. However, this dye degrades at temperatures around 100 °C and therefore the reaction that chemically links the stabiliser to the spheres can not be performed [29].

The third method to stain the PMMA is to add the fluorescent dye after particle synthesis. This is achieved by finding a solvent that will dissolve the dye and also be taken up by the particles. Thus, an acetone/cyclohexanone mixture can be used to deliver rhodamine perchlorate dye to preformed PMMA spheres [13]. The advantage of this method is that once a suitable delivery system is found, many possible dyes, and even multiple dyes, may be added to the spheres. The disadvantage is that the solvent mixture may attack the spheres, swell them or alter their physical properties.

An advantage of PMMA spheres is that the polymer may be cross-linked [30]. This is achieved via a molecule with two polymerisable groups which is used to chemically bind all the individual PMMA polymer chains in a particle together into a network. This can stabilise the particles in solvents which would normally dissolve them such as aromatics. An additional benefit is that this method allows the fluorescent dye to be kept within one particular area of the particle, usually its core. The preparation of such core-shell particles [27, 31, 32, 33] involves modifying the usual reaction by adding the cross-linking agent and dye at the start of the procedure and creating particles as usual. However, instead of going on to chemically link the stabiliser to the particles, they are cleaned to remove excess dye and then more methyl

methacrylate monomer and cross-linking agent are reacted with them to produce an undyed shell. The stabiliser is then chemically attached. Such core-shell particles allow for more accurate detection of the particle centers from microscopy in concentrated systems, as the fluorescent cores are well separated from each other (e.g. [34]).

To achieve good imaging conditions in the bulk of the sample and reduce scattering of the laser and excited light, the refractive index (RI) of the particles and the solvent should be closely matched. For PMMA spheres the RI is around 1.5 and can be matched using a mixture of cis-decahydronaphthalene (RI=1.48) and tetrahydronaphthalene (RI=1.54) in a ratio of approximately 2:1. In earlier work [6] a decalin-carbon disulphide mixture was used (ratio 2.66:1) but this is problematic due to the volatility and toxicity of the carbon disulphide. The particle RI may also be modified by a few per cent by adding different monomers during preparation [35].

Another concern when studying colloidal dynamics is sedimentation. To counter this phenomenon, solvent mixtures have been sought which not only index-match the colloids but also allow density matching. Adding carbon tetrachloride [36] to the cis-decahydronaphthalene/tetrahydronaphthalene system was tried but had only limited success as it enhanced photobleaching and imparted a charge to the particles. Another mixture used consists of cis-decalin and cycloheptylbromide (CHB) [36, 37] (or cyclohexylbromide [38]). This also imparts a charge to the colloids, likely due to photo-induced cleavage of the Br-C bond and subsequent solvent acidification, but this may be screened by the addition of salt [39, 40], (partly) restoring the nearly-hard-sphere nature of the system.

For both RI and density matching, it is important to note that the extra solvent components can swell the PMMA particles, and the solvent uptake may take up to weeks to saturate. Time-dependent monitoring is the only sure means of ensuring that the particle size has stabilised. Otherwise, significant errors in volume fraction estimation may result.

Besides PMMA particles, various other systems have been considered in the literature for use in confocal microscopy. One of the best known is silica spheres. They are prepared by the hydrolysis and condensation of alkyl silicates in ethanol using ammonia as catalyst as first described by Stöber *et al.* [41]. They can be made fluorescent by adding dyes that have been reacted with silane coupling agents which make them affix to the silica [42, 43, 44, 45]. The advantage of this system is that various dyes can be used and added at any time during the synthesis [42]. The spheres are stabilized in organic solvents via a dense layer of organophilic material grafted onto their surface [46, 47, 48, 49], and the RI can be matched with the solvent (RI=1.45 for Stöber silica spheres). However, the main problem with silica spheres is that they are quite dense (reported values range from 1.51g/cm<sup>3</sup> [49] to 2.2g/cm<sup>3</sup> [50]) so that sedimentation

problems may be severe with all but the smallest spheres.

Water-based fluorescent particles can also be used, but their RI differs considerably from that of water, limiting observation in the bulk. The RI of water can be modified by adding salts [51], but the concentrations required are exceptionally high, making most particles unstable against van der Waals attraction.

A final interesting development is that of quantum-dot-loaded particles. Quantum dots [52] are themselves very small semiconducting colloids (1 nm to 10 nm) which fluoresce due to quantum confinement. They can be trapped within a polymer or silica [53] colloid. Since quantum dots photobleach much less than organic dyes, they can be used for experiments involving long-term observation.

## B. Imaging

Direct imaging dates back to the work of Robert Brown [54], who used it to discover and study Brownian motion, which is *the* defining characteristic of colloids. Subsequently, Perrin [55] used direct imaging to great effect in his Noble-Prize-winning work on sedimentation equilibrium and diffusion in *dilute* suspensions. However, direct imaging has flourished as a major research tool in colloidal research only in the last two or three decades, mainly due to the increase in imaging and computing power.

Our main emphasis in this article is on high-resolution imaging and reconstruction of the position of *every* particle in some volume of a concentrated colloidal suspension under flow in real-time. Before reviewing this subject in detail, we point out the use of conventional, low-resolution imaging to track the position of a number of *tracer* particles. Perhaps most important for our purposes here, the well-established technique of particle imaging velocimetry (PIV) [56] can be used to shed light on complicating factors in conventional rheological measurements such as wall slip [57, 58] and flow non-uniformities such as shear banding [59]. Thus this technique has recently been used in a rheometer to elucidate the physics of wall slip in concentrated emulsions under shear [60, 61]. The correlation techniques used in PIV to measure tracer velocity can also be used to track the shear-induced diffusion of tracers in concentrated suspensions of non-Brownian spheres [62, 63]. PIV and related techniques are, of course, limited to transparent samples.

For completeness, we mention other methods for velocimetry that have no requirement for transparency, such as heterodyne light-scattering [64] and ultrasonic velocimetry [65]. The latter has been applied to characterise slip and flow non-linearities in micelles and emulsions [66, 67]. We also mention under this heading Nuclear Magnetic Resonance Imaging (NMRI) [68, 69, 70, 71], another velocimetry method independent of transparency, which can also provide information on local density. The technique has spatial resolution down to  $\sim$

20  $\mu\text{m}$  and has been combined with rheometric set ups to relate velocity profiles to macroscopic rheology [72, 73], to give insight on the occurrence of shear bands [74] and shear thickening [75] in concentrated suspensions.

While all of these techniques give additional insight unavailable from bulk rheology alone, building up a complete picture of colloidal flow requires dynamical information on the single-particle level. We now turn to microscopic methods that give precisely such information. We focus on single-particle imaging in 3D, but mention that the imaging of a single layer of colloids has been used to great effect to study fundamental processes in 2D (e.g. [76, 77, 78]). While perhaps somewhat less complex than 3D imaging, 2D imaging nonetheless presents some challenges, e.g. when the imaged objects come into very close proximity [79].

The use of conventional (non-confocal) optical microscopy to study concentrated colloidal suspensions in 3D has been reviewed before [80]. In nearly index-matched suspensions, contrast is generated using either phase contrast or differential interference contrast (DIC) techniques. One advantage of conventional microscopy is speed: image frames can easily be acquired at video rate. Conversely it has poor ‘optical sectioning’ due to the presence of significant out-of-focus information, so that particle coordinates in concentrated systems cannot be reconstructed in general, although structural information is still obtainable under special circumstances [81].

Compared to conventional microscopy, confocal microscopy delivers superior ‘optical sectioning’ by using a pinhole in a plane conjugate with the focal ( $xy$ ) plane. It allows a crisp 3D image to be built from a stack of 2D images even for somewhat turbid samples, but each 2D image is acquired by scanning, which imposes limits on acquisition speed. The technique has been described in detail before [82].

The use of confocal microscopy to study concentrated colloidal suspensions was pioneered by van Blaaderen and Wiltzius [83], who showed that the structure of a random-close-packed sediment could be reconstructed at the single-particle level. Confocal microscopy of colloidal suspensions in the absence of flow has been recently reviewed [13, 14, 15, 16]. We refer the reader to these reviews for details and references. Here, we simply note that this methodology gives direct access to *local* processes, such as crystal nucleation [84] and dynamic heterogeneities in hard-sphere suspensions near the glass transition [34, 37].

Our main interest is the use of microscopy to study the flow of concentrated suspensions at single-particle resolution in 3D. It is possible to use conventional (non-confocal) video microscopy for this purpose [85, 86, 87, 88], but the poor optical sectioning hinders complete, quantitative image analysis. Conversely, crisp confocal images in principle permit the extraction of particle coordinates, but due to slow scanning and acquisition rates, early observations in real time (i.e. during shear) produced blurred images that again limited the potential for

quantitative analysis [89]. A common solution was to apply shear, and then image immediately after the cessation of shear, both in 2D [90, 91] and in 3D [89, 92, 93, 94]. In the next subsection we review developments in confocal microscopy that permit faster acquisition and hence time-resolved 3D imaging of particulate systems under flow.

### 1. Confocal microscopy

Confocal images are built by scanning a laser beam across the field of view and collecting the emitted fluorescent light through a pinhole (Laser Scanning Confocal Microscopy, LSCM). Traditionally the laser beam is scanned across the specimen by two galvo-mirrors which gives maximum acquisition rates of the order of 1 Hz, depending on image size. Technical advances such as the use of resonant galvo-mirrors, spinning (Nipkow) discs (possibly extended with an array of micro-lenses) and acousto-optic deflectors (AODs) have significantly improved upon such acquisition rates.

AODs are crystals which act as diffraction gratings. By sending a standing sound wave at radio-frequency across the crystal the local index of refraction is changed, creating a grating which deflects laser beams passing through the crystal. By changing the frequency of the sound wave, the diffraction angle is changed and therefore the field of view can be scanned extremely rapidly. The main problem associated with AODs is that the grating deflects light of different wavelengths by different angles and therefore obstructs the fluorescent light travelling back along the optical path. This is partly resolved by combining an AOD with a galvo-mirror and a slit instead of a pinhole. The galvo-mirror positions the beam in one direction, the AOD scans in the orthogonal direction and the fluorescent signal is detected through the slit. The slit slightly reduces the rejection of out-of-focus light and causes a slight anisotropy in the in-plane point-spread function, but the method offers frame rates  $\gtrsim 100$  Hz for  $512 \times 512$  pixels images.

Another technique that improves the scanning speed is the use of a spinning (Nipkow) disc [82]. This solution operates by illuminating the sample through an array of pinholes printed onto a spinning disc and thus achieving the scanning of the sample during the disc's revolution. Spinning discs can achieve full scanning of the field of view by fractions of a revolution and therefore yield frame rates of hundreds of Hz. Disadvantages of this method are the fixed size of the pinholes, limiting the use of different objectives for optimum operation, and also the strong loss of intensity occurring at the disk. Recently, the last disadvantage has mostly been overcome by using laser illumination in combination with an additional array of micro-lenses, strongly increasing the efficiency and considerably reducing photo-bleaching [95].

Regardless of the scanning principle, the confocal microscope can be operated either in a 2D mode, i.e. cap-

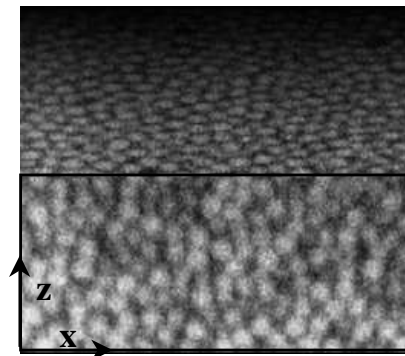


FIG. 3: Reprinted from [96]. Projection of a raw 3D image stack of  $1.7 \mu\text{m}$  PMMA particles. The image volume,  $x \times y \times z \sim 29 \times 29 \times 15 \mu\text{m}^3$  ( $256 \times 256 \times 76$  voxels), was scanned in  $\sim 1$  s.

turing time sequences of images at a fixed focal depth  $z$ , or in a 3D mode, i.e. capturing image stacks obtained by scanning the sample volume, Figure 3. For rapid 3D acquisition, the best method of scanning along  $z$  is to use a piezo-element for focus control of the objective. The two operation modes impose different limits on the acquisition rates for successful quantitative imaging (see Section III B and [96]).

### C. Flow geometries

Microscope studies of flowing particulate suspensions, and soft matter systems in general, require well-defined flow geometries to facilitate data interpretation and allow, in principle, for a mapping of the observed dynamics to the rheological properties of the system. To date, many studies have employed flow cells which impose the deformation (rate) but do not have the ability to measure directly the (shear) stress. Recently this limitation has been overcome by combining confocal imaging with a rheometer and by inferring (indirectly) stress from pressure drops in channel flows.

In all geometries, wall properties play a crucial role in the application of shear. The most direct manifestation of wall effects is that of (apparent) slip in many complex fluids, in particular colloid gels or pastes driven along smooth surfaces [60, 61, 97]. While the physics of slip in suspensions and pastes is an interesting topic in its own right (see Section IV A 1), in most flow geometries the practical goal is to minimise slip and transfer shear to the suspension. The remedy for wall slip differs between various systems; for moderate to very dense particle suspensions, a coating consisting of a sintered monolayer of similar size particles generally provides stick boundary conditions.

### 1. Parallel plate shear cells

Planar shear, or planar Couette flow, is simply implemented by placing the material between two parallel plates much larger than their separation  $z_{gap}$ , and translating them relative to each other. This can be achieved either by fixing one of the plates and moving the other one, or by moving them in opposite directions so that, in the laboratory frame, the zero velocity plane is situated somewhere between the two plates. For a Newtonian fluid without slip and sufficiently far from the edges of the plates (a few  $z_{gap}$ ), the shear rate in the fluid is constant,  $\dot{\gamma} = (v_T - v_B)/z_{gap}$ , with  $v_T$  ( $v_B$ ) the top (bottom) plate velocity. In the following, we denote the shear velocity direction by  $x$ , the vorticity direction by  $y$  and the velocity gradient direction by  $z$ .

By construction, parallel plate shear cells can only achieve finite strains after which the direction of motion must be reversed; they are thus particularly suited for oscillatory strain studies. However, in some designs, extremely large strains are possible ( $\sim 20 - 50$ ) so that, with constant drive velocity, steady shear is effectively achieved in each half-cycle. Using a microscope glass (cover) slide as the bottom plate allows imaging of the suspension during shear. An important requirement is that the plates should be strictly parallel; this condition is particularly stringent for small plate separations e.g. [98]. Non-parallel plates induce non-uniform shear as well as drifts in the sample due to capillarity effects. Other considerations relate to component weight, mechanical resonances, the driving motor and minimising sample evaporation. Depending on the desired operation range, compromises may be required to optimise either long-time stability or high-frequency behaviour.

Planar shear cells were initially coupled to conventional microscopes [85, 86] or light scattering set ups [86, 99, 100, 101]. With the advance of confocal imaging they are now preferentially used in combination with an inverted microscope and a confocal scanner.

Cohen *et al.* [102, 103] used a simple design with a movable microscope cover slip as lower plate and a fixed top plate. The maximum plate separation  $100 \mu\text{m}$  and they were parallel to within  $1 \mu\text{m}$  over the shear zone. The lower plate was driven by a piezoelectric actuator with displacements up to  $90 \mu\text{m}$  at frequencies  $\leq 100 \text{ Hz}$ . The sample between the plates was in contact with a large reservoir of un-sheared bulk suspension.

A similar design but allowing for larger strains and higher shear rates is described by Solomon *et al.* [94]. Two tilt goniometers allow the user to tune the parallelism of the plates; a gap of  $150 \mu\text{m}$  is set by a linear micrometer. Oscillatory shear was produced by applying a sinusoidal displacement with a linear stepper motor. The shear rates were in the range  $0.01 - 100 \text{ s}^{-1}$  and strain amplitudes in the range  $0.05 - 23$ .

A cell optimised for slow shear and large amplitudes was developed by the Edinburgh group [96, 104]. The operational gap size ranged from  $\sim 200 - 1000 \mu\text{m}$  with

plates parallel to  $\pm 5 \mu\text{m}$  over the shear region. The top plate was driven at  $0.05 - 10 \mu\text{ms}^{-1}$  by a mechanical actuator with magnetic encoder. The maximum translation was  $L_s \sim 1 \text{ cm}$ , allowing steady shear up to a total strain  $\Delta\gamma = L_s/Z_{gap} \gtrsim 1000\%$ . The cell could be operated either with the bottom plate fixed or with the plates counter-propagating via an adjustable lever system to tune the zero velocity plane.

A recent, ‘state of the art’, parallel plate cell is the design by Wu *et al.* [98], which combines high mechanical stability and a modular construction. The plate separation ranges between  $20$  to  $200 \mu\text{m}$ , and a special pivot system was designed to align the plates parallel to the highest degree. A piezo-stepper motor provided plate velocities ranging from  $\sim 2 \mu\text{ms}^{-1}$  to  $10 \text{ mms}^{-1}$ . As in the Edinburgh’s design, the relative plate motion can reach up to  $\sim 1 \text{ cm}$ , allowing for large accumulated strain ( $\lesssim 50$ ) and quasi-steady shear.

### 2. Rotational geometries

Application of continuous shear is achieved in rotational geometries such as cylindrical Couette, plate-plate or cone-plate devices, the standard geometries used in traditional rheology [105]. Of these, cone-plate and plate-plate geometries are most suitable for microscopic observation. Various ways of conventional (microscopic) imaging in such geometries have been used, including an early direct observation of crystallization in a plate-plate rheometer [106] and a microscopic study of a confined, charged suspension under continuous shear in a rotational plate-plate set-up [87]. Another technique is to image tracer particles in the system from the side of a cone-plate or plate-plate geometry to obtain the deformation or velocity profile. This has been done both qualitatively [107] and quantitatively [61].

For completeness we also mention geometries used to study non-Brownian suspensions, where the typical dimensions are much larger (particle radius  $a \gtrsim 50 \mu\text{m}$ ). One is an annular channel formed by two concentric glass cylinders where a ring-shaped top plate drives the suspension [108], the other consists of a special truncated counter-rotating cone-plate cell [63]. Both set ups allow for imaging in multiple directions using different camera positions. As an exponent of imaging with multiple cameras, we mention the recent work in [109], where two orthogonally positioned cameras were used simultaneously to image tracers in an immersed granular packing sheared in a cylindrical Couette cell. Analysis of the data from the two cameras provided the full three-dimensional trajectory of the tracers.

The first combination of a rotational shear cell with confocal microscopy was described in [110, 111]. It consists of a cone-plate, similar to Figure 4(b), where the cone and the plate (a large glass cover slide) could be rotated independently. In contrast to Figure 4(b), the objective was located at a fixed radial position where

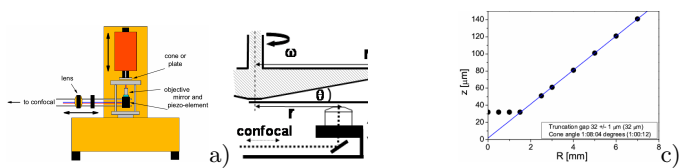


FIG. 4: Reprinted from [96]. (a) Schematics of the confocal rheoscope of the Edinburgh group [96]. The top arrow marks translation of the rheometer head to adjust the geometry gap, the horizontal arrow indicates translation of the arm supporting the objective to image at different radial positions  $r$ . (b) Close up of the central part of the rheoscope, similar to the cone-plate imaging system of Derks [111] except that in the latter the lower plate can also be rotated, while in the former the microscope objective radial position  $r$  can be varied. (c) Gap profile of a  $1^\circ$  cone-plate geometry, measured in the confocal rheoscope with fluorescent particles coated on both surfaces.

the gap height was 1.7 mm. This exceeds the working distance of high numerical aperture objectives so that only the lower part of the gap could be imaged at single-particle resolution, a general limitation of any large-gap geometry. The shear rates obtained were in the range of  $10^{-2}$  to  $10^2$   $\text{s}^{-1}$ . The height of the zero velocity plane could be adjusted by tuning the ratio of the cone and plate rotational speed, while keeping the shear rate constant. Due to the weight of the cone and plate, oscillatory shear experiments were limited to low frequencies. The main limitation of this set up is the acquisition rate of the confocal scanner: particle tracking could be achieved only near the zero velocity plane and in systems where the out-of-plane motion was slower than the acquisition rate, such as a colloidal crystal.

A more recent development of confocal imaging in a ‘rheometric’ geometry, which also permits simultaneous measurement of the rheological properties, is the set up of Besseling *et al.* [96], see Figure 4. Here a rheometer was equipped with a custom-built, open base construction, providing space for imaging optics. An adjustable plate with an imaging slit at the top of the base is covered with a circular cover slide forming the bottom surface of the geometry. This allows for imaging at various radial distances  $r$ . The stress-controlled rheometer (AR2000, TA instr.) enables all classical rheological tests either in plate-plate or cone-plate geometry. In practice a cone with an angle of  $1^\circ$  was used, Figure 4(b),(c). The imaging optics under the plate (piezo-mounted objective to scan along  $z$ , mirror and lenses) are coupled to a confocal scanner (VTEye, Visitech) to give full 3D imaging capabilities as in a standard microscope mount. A major advantage is the acquisition rate (200 fps) of the confocal scanner, which allows 3D imaging of single particle dynamics up to rates of  $\sim 0.1$   $\text{s}^{-1}$  and measurements of in the  $xy$  plane up to  $100$   $\text{s}^{-1}$ . Finally, either the cone or the bottom glass plate (or both) can be coated with a sintered layer of colloidal particles for the study of slip-related problems.

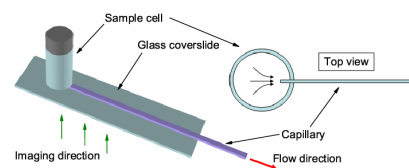


FIG. 5: A possible sample cell for capillary flow. The capillary is not drawn to scale. The construction is placed on the microscope stage and imaged from below.

### 3. Capillaries and micro-channels

Micro-channels and capillaries are flow geometries that occur in many practical applications. They are also interesting from a fundamental perspective, offering insight on issues such as flow instabilities [112], confinement [113] and particle migration effects [114, 115, 116, 117]. When the pressure drop over the channel is measured, it is possible, in principle, to relate microscopic observations to bulk rheological properties (see e.g. [118]), but this is non-trivial as it requires steady, uniform flow along the channel and absence of entrance or confinement effects [119].

From the 1970s, a large number of imaging studies of non-Brownian suspensions flowing in mm- to cm-sized channels have been performed via Laser Doppler Velocimetry [120, 121, 122, 123] and Nuclear Magnetic Resonance Imaging [124, 125], but very little structural information has been obtained at the single-particle level. Optical microscopy experiments on channel flows of colloids have only recently started to appear, often in relation to microfluidics applications [126]. To avoid image distortions, channels with square or rectangular cross sections are generally preferred to cylindrical capillaries.

Haw [112] studied the jamming of concentrated hard-sphere colloids at the entrance of mm-sized, cylindrical capillaries using conventional microscopy. The shape of the channels and the method of imaging militated against accessing detailed microscopic information.

Confocal studies in the group of Weeks [116, 117] used rectangular capillaries ( $50\mu\text{m} \times 500\mu\text{m}$ ) coupled to a syringe as a reservoir to drive suspensions of intermediate volume fractions. Due to the high flow rates involved in their experiments, particle tracking was impossible and instead the flows were studied using image correlation techniques and intensity measurements. A very similar geometry, but with square channels was used in [127] to study the flow of attractive gels of silica particles.

Isa and co-workers [96, 128, 129] used a slightly different geometry to study the flow of very dense colloidal pastes. Figure 5 shows a sketch of the setup: square or rectangular, micron-sized glass capillaries are connected to a glass reservoir at one end and flow is driven by suction at the other end of the channel. The capillaries are either untreated and smooth, or have the inner walls coated with a sintered layer of PMMA colloids.

The recent development of micro-fabrication tech-



niques (soft lithography) has opened up the possibility of studying flow in microfluidics geometries. Degrè *et al.* [118] have performed PIV studies of polymer solutions seeded with tracers in micro-fabricated geometries made by adhering a moulded block of polydimethylsiloxane (PDMS) onto a glass cover slide, obtaining channels with a thickness of tens of microns. PDMS has many practical advantages, but swells in most organic solvents [130], making it incompatible with many colloidal model systems. It also has a relatively low elastic modulus causing deformation under high pressures. A solution to these problems is to substitute PDMS with a photo-curable monomer, as described in [131]. It is clear that soft lithography offers great flexibility in designing channels of almost any geometry, paving the way for high-resolution imaging studies of colloidal flows in a variety of complex micro-environments. Such studies will be relevant for microfluidic applications, as well as for modelling flows in porous and other complex materials.

### III. IMAGE ANALYSIS

To extract the maximum amount of quantitative information from (confocal) images, detailed image analysis is necessary. The central components of such analysis are particle location and tracking.

#### A. General methods

The basic method to obtain coarse-grained information on the flow without details on the dynamics at the particle level is Particle Image Velocimetry (PIV) or related correlation techniques [56]. Using a sequence of images of tracer particles in the suspension or confocal images of the full microstructure during flow, a map of the advected motion between consecutive 2D images,  $i - 1$  and  $i$ , or between parts of these images ('tiles'), is obtained as the shift,  $(\Delta X, \Delta Y)$ , which maximizes the correlation between these images or regions. By repeating the procedure over a sequence of frames, one obtains the displacement as function of time,  $(\Delta X(t_i), \Delta Y(t_i))$ . In general, PIV yields a discrete vector field,  $\Delta \mathbf{R}(\mathbf{r}_{pqr})$ , with displacement  $\Delta \mathbf{R}$  in each element  $\mathbf{r}_{pqr}$  of a 3D image ( $\mathbf{r}_{pq}$  in 2D). In many practical cases however, the flow field has a simpler structure, see the examples in Figure 6.

For 2D images with uniform motion in the  $xy$  plane, the procedure is applied to the entire image, Figure 6(a), giving  $\Delta \mathbf{R}(\mathbf{r}, t_i) = \Delta X(\mathbf{r}, t_i) = \Delta X(t_i)$ . For advective motion which depends on the position  $y$  transverse to the flow, Figure 6(b), the procedure is performed on image strips, yielding  $\Delta X(y_q)$  discretised at the strip centers  $y_q$ . For 3D images of simple shear, Figure 6(c), the motion is a function of  $z$  only. The image stacks are then decomposed in  $xy$  slices at different  $z$  and the procedure is applied to the individual 2D slices. In channel flow,

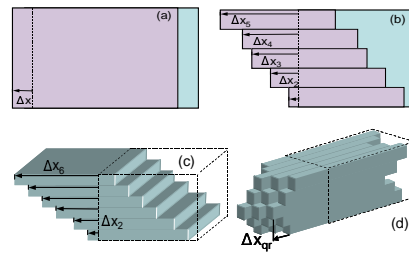


FIG. 6: Reprinted from [96]. Advection profiles in various geometries. (a) A uniform 2D shift  $\Delta X$  across the entire field of view maximises the correlation. (b) 2D case where the advected motion is a function of  $y$ ; the image is then decomposed in bins centered at  $y_q$ , each of which is shifted by  $\Delta X(y_q)$  to obtain maximum correlation. (c) 3D image where the motion is a function of  $z$  only. The stack is decomposed in slices centered at  $z_r$ , each of which is shifted by  $\Delta X(z_r)$  to maximize the correlation. (d) 3D case with  $y$  and  $z$  dependent motion. Decomposition into  $y$  and  $z$  bins yields the advection profile  $\Delta X(y_q, z_r)$ .

Figure 6-d, the stacks are first decomposed in  $xy$  slices and then each slice is decomposed in  $y$ -bins for which the motion is analysed.

These methods have been used to measure the velocity profiles in various dense suspensions. Meeker *et al.* [60] imaged tracers embedded in pastes from the edge of a cone-plate geometry. A number of studies have been reported in which micro-PIV is applied to the flow in channels [118, 132] or to obtain displacement profiles in parallel plate geometries [102].

A related application of the correlation method has been reported by Derks and co-workers [111]. In their study of dense colloids flowing in a cone-plate geometry, a single confocal scan in the velocity-gradient plane ( $y - z$  plane in their notation, see Figure 7) was performed. This was then analysed by shifting and correlating *lines* (along  $y$ ) between consecutive  $z$ -values in the image, rather than performing PIV between consecutive frames. Via this procedure the distortion of the particle images could be quantified, yielding parabolic displacement profiles, Figure 7, corresponding to linear velocity profiles from which the shear rate was extracted.

#### B. Locating particles

To go further in the analysis, one first needs to determine the location of the particle centers from the images. The standard method was developed over a decade ago by Crocker and Grier (CG) [133], and has since been used in numerous studies on colloidal dynamics.

While some of the concepts in their method may also apply to identifying objects with varying shapes [134], the method is primarily aimed at identifying circular (2D) or spherical (3D) objects that appear bright on a dark background. Since experimental images have unavoidable pixel noise and often also undesired intensity

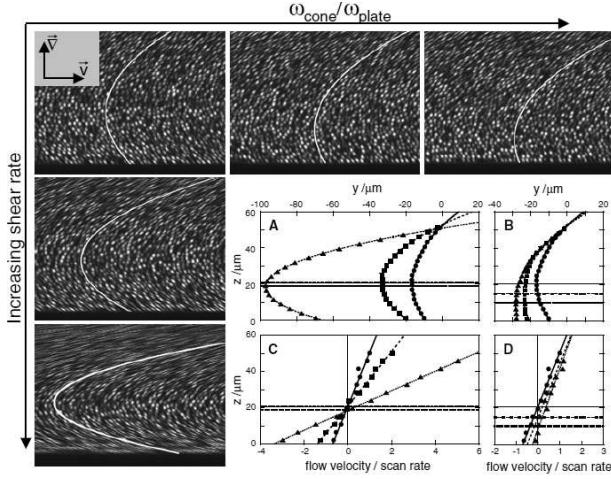


FIG. 7: Reprinted with permission from [111], copyright [2004], Institute of Physics Publishing. Confocal images ( $yz$ ,  $75 \mu\text{m} \times 56 \mu\text{m}$ ,  $512 \times 512$  pixels<sup>2</sup>) of a colloidal fluid at various shear conditions taken in the counter-rotating cone-plate shear cell [111], see Section II C 2. The applied shear rates are  $1.67$ ,  $3.36$  and  $8.39 \text{ s}^{-1}$  (top to bottom); the ratios of the applied cone to plate rotation speeds are  $84$ ,  $129$  and  $175$  (left to right). Graphs A and B show displacement profiles,  $y(z)$ , measured from these images via cross-correlation of scanned lines. The appropriate profile is overlaid on each image (white curves). The velocity profiles ( $dy/dz$ ) calculated from these displacement profiles are shown in the graphs C and D. The particle diameter is  $1.50 \mu\text{m}$ .

modulations, the images are first treated with a spatial bandpass filter, which eliminates long-wavelength contrast gradients and pixel-to-pixel noise. Next, the coordinates of the centers of the features are obtained by locating the local intensity maxima in the filtered images. These coordinates are then refined to a higher accuracy by applying a *centroiding* algorithm, which locates the brightness-weighted center of mass (centroid) of the particles; with this refinement the coordinates of the particle center can be obtained with a typical resolution of  $1/n$  of the pixel size [133] where  $n$  is the particle diameter in pixels. However, the method has some limitations in concentrated systems, as individual particle images may start to overlap. Unless one uses the core-shell particles mentioned in Section II A, an alternative method to the coordinate refinement may be required. A very useful technique for doing this, based on optimizing the overlap between the measured intensity profile of each particle and the so called ‘sphere spread function’, has been described recently by Jenkins and Egelhaaf [135].

In addition to the intrinsic sub-pixel accuracy from the above refinement methods, additional errors arise also from particle motion during image acquisition. These errors may be considerable when images are obtained by a scanning system, where the pixels are not acquired instantaneously. For an acquisition time  $1/f_{\text{scan}}$  for a 2D image with  $n$  lines and a particle radius (in pixels) of  $\tilde{a}$ ,

the acquisition time of a particle image is:

$$t_{\text{im}}^{2D} = 2\tilde{a}/(nf_{\text{scan}}). \quad (1)$$

For a 3D image (a  $z$ -stack of 2D slices), the voxel size in the  $z$  direction may differ from that in the  $x$  and  $y$  direction. When the particle radius in  $z$ -pixels is given by  $\tilde{a}_z$ , the acquisition time for a 3D particle image is:

$$t_{\text{im}}^{3D} = 2\tilde{a}_z/f_{\text{scan}}. \quad (2)$$

Typical parameters ( $f_{\text{scan}} = 90 \text{ Hz}$  in a fast confocal,  $n = 256$ ,  $\tilde{a} = \tilde{a}_z = 5$ ) yield  $t_{\text{im}}^{2D} \simeq 0.4 \text{ ms}$  and  $t_{\text{im}}^{3D} \simeq 0.1 \text{ s}$ .

The additional errors resulting from this finite acquisition time are easily estimated. We do so here for hard spheres (HS). The short time diffusion leads to an error  $\delta_{HS} = \sqrt{D_s(\phi)t_{\text{im}}/2}$ . Here  $D_s(\phi)$  is the volume fraction ( $\phi$ ) dependent short time diffusion constant for hard spheres:  $D_s(\phi) = (k_B T)/(6\pi\eta a)H(\phi)$  with  $H(\phi) < 1$  a hydrodynamic correction [7, 136, 137, 138, 139]. Note that this is an upper bound applicable to HS; for colloids with softer interactions,  $\delta < \delta_{HS}$ . With a solvent viscosity  $\eta \simeq 3 \times 10^{-3} \text{ Pa}\cdot\text{s}$ , and frame rates as above, typical values are  $\delta_{2D} \simeq 2 \text{ nm}$  and  $\delta_{3D} \simeq 35 \text{ nm}$  for a colloid with radius  $a = 1 \mu\text{m}$ . For 3D imaging, this error exceeds the intrinsic sub-pixel accuracy. Further errors due to flow-induced distortion of the particle image are estimated by comparing the imaging time  $t_{\text{im}}$  with the time  $t_f$  required for the flow to displace the particle over its own diameter. For a flow velocity  $\tilde{V}$  (in pixels per second),  $t_f = 2\tilde{a}/\tilde{V}$ . We consider the particle significantly distorted if  $t_{\text{im}}/t_f \geq 0.1$ . Hence, using Eqs. 1,2, the maximum velocities are:

$$\tilde{V}_{2D}^{\text{max}} = 0.1nf_{\text{scan}}, \quad \tilde{V}_{3D}^{\text{max}} = 0.1f\tilde{a}/\tilde{a}_z. \quad (3)$$

Using the above parameters, a typical maximum velocity in 2D is  $V^{\text{max}} \simeq 500 \mu\text{ms}^{-1}$ , while for 3D images with  $\tilde{a}/\tilde{a}_z = 1$ , we obtain  $V^{\text{max}} \sim 2 \mu\text{ms}^{-1}$ . In both cases, further improvement could be achieved by removing the distortion prior to locating the particles by correlating scanned images or lines at different  $z$  [111].

### C. Tracking algorithms

Merging particle coordinates from subsequent frames into single-particle trajectories is the optimal route to analyse colloidal dynamics. However, in some cases this is difficult [140], but quantitative information may still be obtained via alternative methods. For example, Breedveld *et al.* [62, 140, 141] measured the distribution of all possible displacement vectors in images of tracer particles in dense non-Brownian suspensions. From these distributions, the contribution due to cross correlations, corresponding to vectors connecting the position of particle  $i$  in one frame to that of particle  $j$  in the next frame, could be subtracted. From the resulting autocorrelation part of the distribution, the full shear-induced self-diffusion

tensor could be obtained. While this method also has potential for analysis of coordinate ensembles obtained from (confocal) microscopy during flow, we will focus on a complete analysis of the particle dynamics via tracking.

### 1. Conventional Tracking

The most widely used algorithm to track particles from ensembles of coordinates in consecutive frames is that of Crocker and Grier (CG, [133]). It is based on the dynamics of dilute non-interacting colloids. Given the position of a particle in a frame and all possible new positions in the next frame, within a ‘tracking range’  $R_T$  of the old position, the algorithm chooses the identification with the minimum mean squared frame to frame displacement (MSFD). The algorithm has been used to analyse particle dynamics in a wide variety of 2D and 3D images of quiescent systems, see e.g. [15, 16]. Its main limitation is that, when the particle motion between frames is excessive, misidentifications can occur. Such motion can be due to diffusion, flow-advection or both.

In quiescent systems, the ability to track particles between frames is limited by experimental constraints such as the acquisition rate of the (confocal) microscope, image dimensionality, particle size and concentration, and solvent viscosity. After locating the particles, the relevant quantity which relates to the tracking performance of the CG algorithm is the root mean squared frame-to-frame displacement relative to the mean interparticle distance  $\ell$ . If particles move on average a substantial fraction of  $\ell$ , then the algorithm starts to misidentify them. This has recently been quantified [96] by testing the CG algorithm on computer-generated hard-sphere or hard-disk ensembles at different concentrations. These tests showed that the algorithm can handle larger mean squared displacements (MSDs) for more concentrated systems, since the higher concentration prevents particles from coming into close proximity of each other between frames.

The tests were also performed on computer-generated data in which additional uniform or non-uniform motion was added, to study how far the CG algorithm could be pushed beyond its original design parameters. For uniform motion, CG tracking was as successful as in the quiescent case for small drifts but failed for drifts of the order of half the particle-particle separation. For non-uniform (linear shear) flows with small strains between frames the identification worked correctly, but large non-uniform displacements caused major tracking errors.

### 2. Correlated Image Tracking

Some important limitations to particle tracking in 2D or 3D images with large drift or non-uniform motion (see also [142]) can be overcome by the method of Correlated Image Tracking (CIT), described in detail in [96]. The

main extension compared to conventional (CG) tracking is that, prior to tracking, the time- and position-dependent advective motion is obtained from a PIV-type correlation analysis as in Section III A. This advected motion is then subtracted from the raw particle coordinates, shifting them to a ‘locally co-moving’ (‘CM’) reference frame where the particles can be tracked with the CG algorithm.

Since particle coordinates are distributed continuously, the advection profile  $\Delta\mathbf{R}(x_p, y_q, z_r, t_i)$  from the PIV analysis is first interpolated to obtain a *continuous* profile  $\Delta\mathbf{R}(x, y, z, t_i)$ . Using the latter, the transformation of the position  $\mathbf{r}_k(t_i) = [x_k(t_i), y_k(t_i), z_k(t_i)]$  of particle  $k$  in the laboratory frame to its position  $\bar{\mathbf{r}}_k(t_i)$  in the CM reference frame is:

$$\bar{\mathbf{r}}_k(t_i) = \mathbf{r}_k(t_i) - \sum_{j=1}^i \Delta\mathbf{R}(\mathbf{r}_k(t_j), t_j), \quad (4)$$

with  $\Delta\mathbf{R}(\mathbf{r}_k(t_i), t_j)$  the *past* motion between frame  $j$  and  $j - 1$ , at the *current* particle location  $\mathbf{r}_k(t_i)$ . In the CM frame, the average particle motion is essentially zero over the entire image. Therefore the classic CG algorithm tracks particles successfully in this reference frame. The limitations on the CG tracking performance are essentially the same as discussed in Section III C 1 for quiescent systems. Finally, the resulting trajectories can be restored in the laboratory frame by inverting Equation 4.

The main limitation to CIT originates from the failure of the image correlation procedure when the *relative* particle motion between frames is excessive, rather than from failure due to large absolute shifts between images [96]. This apart, CIT has the same limitations of CG tracking with significant failure for mean squared frame-to-frame displacements in the CM reference of  $\sim (0.3\ell)^2$  in 2D. Two direct applications of CIT will be reviewed in Section IV A.

## IV. IMAGING OF SYSTEMS UNDER DEFORMATION AND FLOW

Direct imaging remains the most detailed method for studying structure and dynamics of particles in flow. This section reviews the application of (confocal) imaging to study flowing concentrated suspensions. We separately discuss disordered systems and systems in which order is present before or as a result of flow. In each case, the focus is on Brownian systems, but we briefly review non-Brownian systems at the end of each subsection.

### A. Disordered systems

#### 1. Slow glassy flows

A significant motivation for recent developments in imaging concentrated colloidal suspensions under flow is

to investigate the behaviour of samples that are so dense that structural rearrangements are arrested in the quiescent (unsheared) state, i.e. colloidal glasses [5]. Elucidating the mechanisms for the deformation and flow of colloidal glasses is currently one of the ‘grand challenges’ in soft matter science. Much insight to this problem can be expected to come from the detailed study of model systems. The simplest model systems are concentrated hard sphere suspensions, which are glassy at volume fractions  $\phi \gtrsim 0.58$ . (This claim has recently been disputed [143]; but however this controversy eventually resolves, it remains true that for almost all practical rheological purposes, amorphous colloidal hard-sphere suspensions behave as soft solids for  $\phi \gtrsim 0.58$ .)

The first time resolved studies of the flow of HS colloidal glasses at single particle level have been described in [96, 97, 104]. Both the 3D particle dynamics and global flow were investigated in steady shear under various boundary conditions using both a planar shear cell and ‘confocal rheoscope’ [97, 104] (geometries with uniform stress in the flow gradient direction  $z$ ). Standard fluorescent PMMA-PHS particles ( $a = 850$  nm,  $\phi = 0.62$ ) in a charge-screened, CHB-decalin mixture were used for observations at the particle scale, measurements on a global scale employed fluorescent tracers in a non-fluorescent host suspension.

We first focus on dynamics observed for rough boundary conditions. Globally, these highly concentrated HS glasses shear non-uniformly, showing rate-dependent shear localization [97, 104, 144]: at the lowest applied rates  $\dot{\gamma}_a$ , the local shear rate  $\dot{\gamma}$  near (one of) the walls considerably exceeds  $\dot{\gamma}_a$  and vanishes smoothly into the bulk where the system remains solid-like. The characteristic length, along  $z$ , characterizing this shear rate variation starts from  $\sim 25$  particle diameters and increases with the applied rate/stress, i.e. the wall ‘fluidization’ propagates into the sample and eventually leads to fully linear flow profile at the largest rate.

The microscopic dynamics inside a shear band was then studied by focussing on a  $30 \times 30 \times 15 \mu\text{m}^3$  volume ( $\sim 3000$  particles) the bottom layer of which was  $\sim 10$  particles away from the wall. A series of undistorted 3D snapshots of the entire microstructure was acquired, from which 3D particle positions and dynamics were obtained as described in Secs. IIIB and IIIC. Particle tracking using the new CIT method allowed to study the flow for *local* shear rates up to  $\dot{\gamma} \simeq 0.05 \text{ s}^{-1}$ . The results are shown in Figure 8, where (a) presents the advected motion  $\Delta X(z, \Delta t)$  (from image correlation) for  $\Delta t = 16$  s and a shear rate  $0.02 \text{ s}^{-1}$  [96]. *Local* velocity profiles such as these are linear on this scale and extrapolate to zero within the resolution, showing the absence of slip in this case. Figure 8(b) shows the distributions  $P(\Delta x)$  and  $P(\Delta y)$ , which are frame-to-frame particle displacements obtained from CIT. The laboratory frame data for the displacements in the velocity direction ( $x$ ) show a large contribution from the advected motion. To focus on the more interesting non-affine part of the dis-

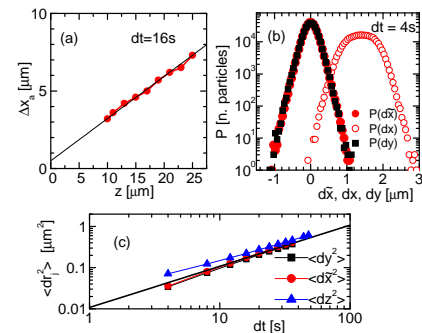


FIG. 8: Reprinted from [96]. 3D analysis of a sheared glass at  $\dot{\gamma} = 0.019 \text{ s}^{-1}$ . (a) (●) accumulated displacement  $\Delta X_a(z, \Delta t)$  (see Figure 6) from image correlation over  $\Delta t = 16$  s (4 frames). Line: linear fit giving an accumulated strain  $d\Delta X_a/dz = 0.28$ . (b) Distribution of frame-to-frame displacements  $P(\Delta x)$  and  $P(\Delta y)$  from Correlated Image Tracking with coordinates restored in the laboratory frame. Also shown is  $P(\Delta \tilde{x})$  of the non-affine  $x$ -displacements, using Equation 5 and  $\dot{\gamma} = 0.019 \text{ s}^{-1}$ . (c) the (non-affine) MSD in the three directions. Line:  $\langle \Delta y^2(\Delta t) \rangle = 2Dt$  with  $D = 5.4 \times 10^{-3} \mu\text{m}^2\text{s}^{-1}$ .

placements,  $\Delta \tilde{x}$ , the  $z$ -dependent advected motion was subtracted via:

$$\Delta \tilde{x}(t) = x(t) - x(0) - \dot{\gamma} \int_0^t z(t') dt', \quad (5)$$

with  $\dot{\gamma}$  measured from the data. The results for  $P(\Delta \tilde{x})$ , Figure 8(b), showed that non-affine motion for  $x$  and  $y$  were very similar. Analysis of the full 3D dynamics further revealed that it is indeed nearly isotropic in all directions, as shown by the long time behaviour of the mean squared displacements for  $x$ ,  $y$  and  $z$  in Figure 8(c). The linearity of these curves at long times also indicates that, after a sufficient number of shear induced cage-breaking events, particle dynamics in the system becomes diffusive, with long-time diffusion coefficients varying by  $< 20\%$  in the three directions.

These experiments give information on individual plastic cage-breaking events as well as rate-dependent structural relaxation. The first phenomenon is illustrated by the non-affine motion of a single particle in the  $\tilde{x} - y$  plane, Figure 9(a). Intermittent jumps, reflecting ‘plastic’ breaking of the particle cages, are observed between periods of ‘rattling’ in which the cage is deformed. An average accumulated strain of  $\sim 10\%$  is found between these events, in reasonable agreement with the yield strain obtained from bulk rheology or light scattering [8, 100]. The changes in the particles’ local environment during shear were also studied via the change in the bond order parameters  $Q_{6,m}^i$  for each particle  $i$  [145] over a time  $dt$ , measured by the quantity  $C_6^i(t, dt)$ , where  $C_6 = 0$  reflects no change. Figure 9(c)-(e) show snapshots of the sheared microstructure at two times, where the grey-scale is proportional to  $C_6^i(t, dt)$ . In Figure 9(c), the changes over 6% accumulated strain are shown. Clus-

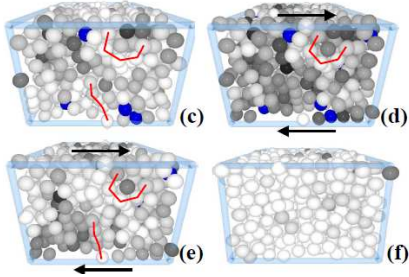


FIG. 9: Partly reprinted from [104]. (a) Trajectory of a single particle over 800 s in the velocity-vorticity plane in the co-moving frame as defined in Equation 5 for a sheared glass at a local shear rate  $\dot{\gamma} = 9.3 \cdot 10^{-4} \text{ s}^{-1}$ . (b) Selected incoherent scattering functions  $F_s(Q_m, t)$ , with  $\dot{\gamma}$  increasing from right to left. The dashed line schematises initial relaxation. Inset: data collapse using  $f_s(Q_m, t/\tau_\alpha)$ , with the line showing that  $f_s \propto \exp(-t/\tau_\alpha)$ . (c-f) Snapshots of the structure for  $\dot{\gamma} = 0.0015 \text{ s}^{-1}$ , (c) at  $t_0 = 80 \text{ s}$  after start of imaging. The grey-scale measures the change in local environment of each particle ( $\propto C_6^2(t_0, dt)$ ) over the past  $dt = 40 \text{ s}$ . (d) at  $t_0 = 120 \text{ s}$  and  $dt = 80 \text{ s}$ . (e) at  $t_0 = 120 \text{ s}$  and  $dt = 40 \text{ s}$ . Red lines show local deformations, arrows mark the shear direction. (f) A quiescent glass, with  $dt = 200 \text{ s}$ .

ters of strong rearrangements, termed ‘Shear Transformation Zones’ (STZs) in earlier theoretical studies [146], can be observed, where the local strain appears much higher than elsewhere. Over the following 6% accumulated strain, Figure 9(e), STZs appear in different locations while the earlier ones remain essentially locked.

The average structural relaxation was examined via the incoherent scattering function,  $F_s(Q, t) = \langle \cos(Q[y_i(t_0 + t) - y_i(t_0)]) \rangle_{i, t_0}$  (using  $Q = Q_m \simeq 3.8a^{-1}$ ). As shown in Figure 9(b), the long-time dynamics is essentially frozen at rest ( $\dot{\gamma} = 0$ ). At short times and small shear rates,  $F_s$  exhibits a plateau corresponding to caging at small accumulated strain. At longer times,  $F_s$  decays to zero due to repeated cage-breaking events in line with the diffusive dynamics in Figure 9(c). This decay accelerates strongly on increasing rate. When scaling time by the characteristic ( $\alpha$ ) relaxation time  $\tau_\alpha$ ,  $F_s$  collapsed onto a single exponential curve (see the inset), which directly confirmed the theoretically predicted time-shear superposition principle.

The rate dependence of the inverse relaxation time and diffusivity  $D$  exhibited a non-trivial scaling:  $D \sim 1/\tau_\alpha \sim \dot{\gamma}^{0.8}$ . Such ‘power-law fluid’ scaling contrasts the yield-stress behaviour observed in the global rheology or predictions from Mode Coupling Theory [147]. (For further

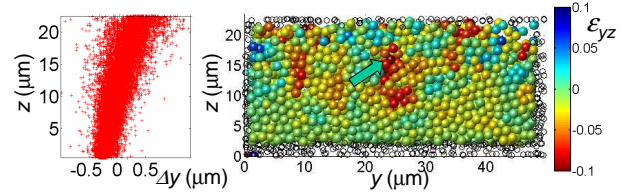


FIG. 10: Reprinted from [152], with permission from AAAS. (A) Shear-induced displacements of particles in a colloidal packing between  $z = 0$  (the cover slide) and  $z = 23 \mu\text{m}$  after 50 minutes of shear (3% average accumulated strain). (B) Strain distribution and shear transformation zones in a  $7 \mu\text{m}$  thick section in the shear-displacement gradient plane. Particle color indicates the value of the local shear strain  $\epsilon_{yz}$  (see color scale), accumulated over 50 minutes of shear. The arrow indicates a shear transformation zone.

discussion of these data in the context of Mode Coupling Theory, see the article by Fuchs in this issue.) However, these observations are consistent with a stochastic non-linear Langevin equation treatment [148, 149]. In this approach to hard-sphere dynamics, particles become more deeply trapped in effective free-energy (or, equivalently, entropic) wells as the concentration increases beyond a certain critical value; the effect of applied stress is to lower the entropic barrier that particles have to surmount in order to escape [150]; the predicted shear-induced relaxation time indeed shows power-law scaling with shear rates in an intermediate regime with exponents close to 0.8 [151].

Subsequently, Schall *et al.* studied the behaviour of dense colloidal packings under very small shear deformations [152]. The packing was formed by sedimentation of silica-spheres ( $a = 0.75 \mu\text{m}$ ) in a lower density solvent, so that the volume fraction varied as function of height. The shear geometry consisted of a movable, coated bottom cover slide, while a metal grid positioned on top confined the packing within a layer of  $42 \mu\text{m}$  ( $\sim 30$  particle diameters). The analysis focussed of the microscopic strain variations resulting from either thermal fluctuations or applied strain. From the thermal distribution of strain energies, an estimate for the shear modulus was obtained, but volume fraction gradients complicate the analysis. Large accumulated local strains were observed at long times in the quiescent sample, indicating aging. The behaviour under application of shear is shown in Figure 10. In this work, the total accumulated strain was  $\sim 3\%$  on average, Figure 10(a), well below the typical bulk yield strain in colloidal hard sphere glasses [8, 100]. Thus, it is probable that the data represent creep rather than yielding and flow.

Figure 10(b) shows a spatial map of the shear strain  $\epsilon_{yz}$  in a slice normal to the shear gradient. The authors identified the localized regions with high strain with STZs, the first published images of STZs in colloidal glasses. Interestingly, the highlighted region revealed a four-fold symmetric strain field just after its (earlier) formation,

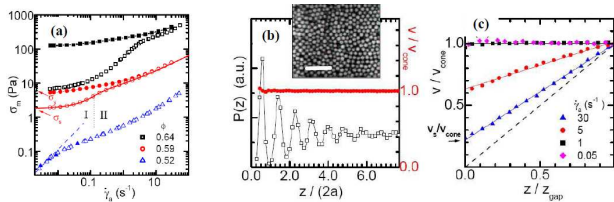


FIG. 11: Reprinted from [97]. (a) Measured stress  $\sigma_m$  versus applied rate  $\dot{\gamma}_a$  for particles with  $a = 138$  nm, at different volume fractions for coated ( $\blacksquare, \bullet, \blacktriangle$ ) and un-coated geometries ( $\square, \circ, \triangle$ ). Dashed line: linearly viscous behaviour. The full line is a flow curve predicted using the model in [97]. Dotted line: applied rate at which yielding starts at the cone-edge. (b) Density profile  $P(z)$  ( $\square$ ), from 3D-imaging of the  $a = 652$  nm system at  $\phi = 0.63$ , during slip at  $r = 2.5$  mm and  $\dot{\gamma}_a = 0.01$  s $^{-1}$ . ( $\bullet$ ) Corresponding velocity profile from particle tracking, showing full plug flow. Inset: Slice of one of the 3D-images, showing the first colloid layer. Scale bar: 10  $\mu$ m. (c) Velocity profiles for the  $\phi = 0.59$  data in (a), in units of the cone velocity  $v_{\text{cone}} = \dot{\gamma}_a \theta r$ , as function of the normalized height  $z/z_{\text{gap}} = z/\theta r$ , for various applied rates  $\dot{\gamma}_a$  at  $r = 2.5$  mm. The arrow marks the slip velocity for  $\dot{\gamma}_a = 30$  s $^{-1}$ ; the dashed line is the behaviour without slip  $v = \dot{\gamma}_a z$  as observed for  $\phi < \phi_G$ .

consistent with theoretical predictions for a single plastic event. Schall *et al.* further identified the STZ-cores and, using somewhat uncontrolled assumptions, calculated the STZ formation energy, activation volume and the activation energy. From this it was concluded that STZ formation was mainly thermally activated, although some strain assistance was involved.

Images such as those shown in Figure 10(b) and 9(c)-(e) show that direct imaging is a very powerful method for studying inhomogeneous local responses to applied stress. In particular, the discovery of STZs in model colloids means that the physics of these systems may have relevance beyond soft matter physics, e.g. in the study of large-scale deformation of metallic glasses [153].

Particulate suspensions and other concentrated soft materials (e.g. emulsions) often exhibit wall slip during flow along smooth boundaries. This is important in practical applications, and strongly relevant when interpreting bulk flow measurements. Slip in particulate suspensions has been seen mostly for high Péclet numbers (non-Brownian suspensions), both in solid- [154, 155] and liquid-like [156] systems. In a recent study, Ballesta *et al.* addressed the effect of Brownian motion and the glass transition on slip in hard-sphere colloids using confocal imaging and simultaneous rheology [97] (Section II C 2). The main results are shown in Figure 11. The rheology for rough walls in Figure 11(a) shows the traditional change from a shear thinning fluid ( $\phi = 52\%$ ) to a yielding solid ( $\phi = 59\%$ ) associated with a glass transition at  $\phi \sim 58\%$  [8, 157]. For a smooth wall and index-matching solvent (which prevents van der Waals attraction and sticking of particles to the glass) the results for a dense liquid remained unchanged, indicating no slip.

This is confirmed by imaging (Figure 11(c), dashed line) and also agrees with earlier velocity profile measurements for dense colloidal liquids [111]. However, for the colloidal glass, a slip branch developed in the flow curve at small rates. This branch was described by a Bingham-form, associated with solid-body motion of the suspension along the glass plate. This ‘solid’ structure during slip was shown to extend down to the first particle layer, Figure 11(b) and the inset, giving microscopic insight in the ‘Bingham’ slip-parameters. The transition from pure slip at low rates to yielding at high rates was also probed, see Figure 11(c). This transition depended on the local gap, i.e. the radial position  $r$ , illustrating the possibility of non-uniform ( $r$ -dependent) stress in a cone-plate.

Interestingly, this slip behaviour of hard-sphere glasses is different in nature from that found earlier by Meeker *et al.* in jammed systems of emulsion droplets [60]. There, a non-linear elasto-hydrodynamic lubrication model, appropriate for deformable particles, could quantitatively account for their observations. It therefore appears that while slip is ubiquitous, the mechanism for its occurrence can be highly system dependent.

## 2. Fast channel flow of fluids and pastes

A different regime of flow in hard-sphere suspensions, either in dense fluids or glasses, occurs when the shear rate becomes comparable to the rate for thermal relaxation of the particles within their cages, which is of the order of the inverse Brownian time. In these situations jamming or shear thickening may start to occur, while in geometries with non-uniform stress, pronounced shear-induced migration may take place. Here we describe recent studies of imaging in this regime, focussing on the specific geometry of capillaries and micro-channels.

The effects of shear-induced migration in intermediate volume fraction hard-sphere suspensions ( $\phi < 0.35$ ) was studied by Frank *et al.* [116] and Semwogerere *et al.* [117]. In these experiments, confocal imaging was used to measure both velocity and concentration profiles,  $\phi(y)$ , of colloids across  $50\mu\text{m} \times 500\mu\text{m}$  glass channels. Flow velocities up to 8  $\text{mms}^{-1}$  were probed, corresponding to Péclet numbers up to  $\sim 5000$ . The gradient in shear rate  $\dot{\gamma}(y)$  causes particles to migrate from the boundaries (with large  $\dot{\gamma}$ ) to the center of the capillary (small  $\dot{\gamma}$ ), resulting in development of a steady state concentration profile beyond a certain ‘entrance length’. Frank *et al.* found profiles (transverse to the flow) where the concentration in the center increased considerably with the average volume fraction or on increasing flow rate (Péclet number, Pe). The data were interpreted via a model which included a shear rate and local volume fraction dependence of normal stresses in the sample. The rapid rise of these stresses with  $\phi$  and Pe was responsible for the observed behaviour. Semwogerere *et al.* [117] studied the entrance length over which the flow became fully developed and found that it increases strongly with

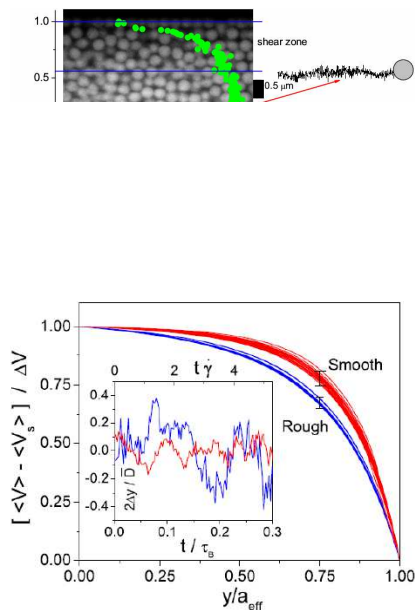


FIG. 12: (a) Velocity profile of a 63.5% volume fraction suspension of PMMA hard-spheres (radius  $a = 1.3\mu\text{m}$ ) in a square, glass micro-channel (side  $2b = 50\mu\text{m}$ ). The velocity  $\langle V \rangle$  is normalized by the centerline velocity  $\langle V_c \rangle$ . The profile is overlaid onto a confocal image of the suspension in the channel. The velocity profile consists of a central, unsheared plug and of lateral shear zones, whose width is highlighted by the horizontal blue lines. The right side of the image shows two examples of particles trajectories in the plug and in the shear zone respectively. The  $x$  and  $y$  scales of the trajectories are different and the colloids are not drawn in scale. (b) Reprinted from [129]. Normalised velocity profiles at  $z = 17\mu\text{m}$  versus  $y/b_{\text{eff}}$  ( $b_{\text{eff}} = b - a$ ) for a wide range of flow rate. For clarity, fits to the data rather than the raw data are shown; the error bars show the spread in the measurements. Inset: normalized transverse fluctuations of individual particles in the shear zone for the two boundary conditions, versus normalized time  $t/\tau_B$  or local accumulated strain  $t \cdot \partial\langle V(y) \rangle / \partial y = t \cdot \dot{\gamma}(y)$ , top axis.

$Pe$ , in marked contrast to non-Brownian flows for which it is flow-rate independent [158]. The entrance length also decreased with increasing volume fraction and the data could be successfully described within their model.

Few imaging studies have been carried out in higher concentration suspensions. Haw [112] observed intriguing behaviour in traditional microscopy studies of PMMA suspensions ( $\phi \gtrsim 55\%$ ) sucked into mm-sized capillaries with a syringe. Strikingly, the volume fraction of the suspension in the capillary was as much as 5% lower than the initial concentration, depending on the particle size. Such unexpected ‘self-filtration’ was attributed to jamming of the particles at the capillary entrance, leading to higher flow rate of the pure solvent under the applied pressure difference.

Motivated by these experiments, Isa *et al.* conducted further studies of flows in similar geometries at the single particle level using confocal microscopy [129]. The system consisted of a hard-sphere suspension (PMMA

spheres, radius  $1.3 \pm 0.1\mu\text{m}$ ) at nearly random close packing, ‘a paste’, in a 20-particle-wide square capillary. The motion of individual colloids was tracked via Correlated Image Tracking and velocity profiles were measured in channels with both smooth and rough walls. Despite the colloidal nature of the suspension, significant similarities with granular flow [159, 160] were found.

The bulk flow curve of the system studied by Isa *et al.* fitted a Herschel-Bulkley (HB) form for a yield-stress fluid [8] at small to moderate flow rates. The velocity profile predicted from a HB constitutive relation consists of a central, unsheared ‘plug’ and shear zones adjacent to the channel walls, which fits qualitatively with what was observed, Figure 12(a). At the same time, however, the size of the central plug is expected to decrease with increasing flow rate, vanishing beyond some critical velocity above which the yield-stress fluid is shear-melted everywhere (see e.g. [105, 161]). But Isa *et al.* found that width of the central plug was independent of applied flow rate, Figure 12(b). This behaviour is analogous to that observed in the pipe flow of dense dry grains [160, 162]. The data for the colloidal flow could be captured by a theory of stress fluctuations originally developed for the chute flow of dry granular media [162, 163]. Presumably, this model can be successfully applied to nearly-close-packed colloidal systems because at high flow rates, inter-particle contacts rather than Brownian motion dominate. Direct imaging showed indeed that the trajectory of a particle in the shear zone was determined by ‘collisions’ with neighbouring particles, Figure 12. Moreover, the presence of rough boundaries enhanced such fluctuations, causing wider shear zones.

In more recent work on the same system [113], using smooth walls, it was shown that confinement can induce instabilities in the flow. Upon decreasing the width of the channels from  $\sim 40$  to  $\sim 20$  particle diameters, the flow developed oscillations above a threshold applied flow rate. Such oscillations consisted of cyclical jamming and un-jamming of the suspended particles and led to filtration effects similar to those reported by Haw [112]. Single-particle imaging was used to demonstrate the presence of a concentration profile across the channel, which was well correlated with the local velocity profile.

### 3. Non-Brownian suspensions

Other recent imaging experiments address the flow of non-Brownian suspensions (i.e.  $Pe \rightarrow \infty$ ) at the single particle level. In a series of papers [62, 63, 140, 141], Breedveld *et al.* investigated the steady shear-induced self diffusion of non-Brownian spheres. They used PMMA particles (radius  $a \sim 45\mu\text{m}$ ) in a RI and density-matching mixture (water, zinc chloride, and Triton X-100, viscosity  $\sim 3.4\text{ Pa s}$ ) and studied suspensions with volume fractions ranging from 20% to 50%. By studying the correlated motion of a small fraction of the particles which had been dyed (Section III C), the self and ‘off-

diagonal' mean squared displacements (MSDs) could be extracted without the use of explicit particle tracking.

For these non-Brownian suspensions, the long-time shear-induced MSD depend on accumulated strain  $\dot{\gamma}\Delta t$  only. The 'long-time' diffusion for  $\dot{\gamma}\Delta t > 1$  is due to the chaotic nature of multiple particle collisions. The associated self-diffusion constants  $D_{xx}$ ,  $D_{yy}$ ,  $D_{zz}$  (in the velocity, vorticity and gradient direction respectively) were found to be anisotropic with  $D_{zz}/D_{yy} < 2$ , while  $D_{xx}$  was almost an order of magnitude larger. The data were in qualitative agreement with hydrodynamic theories and simulations, although quantitative discrepancies remained. In contrast, for the *slowly* sheared glasses in Section IV A 1 [104], which exhibited a non-trivial rate dependence,  $D_{yy}/(a^2\dot{\gamma})$  scales as  $\dot{\gamma}^{-0.2}$ , ranging from 0.7 at low rates to  $\sim 0.3$  at the largest rates, exceeding the result for non-Brownian suspension. A last notable observation in the non-Brownian system in [140] was a regime of reduced diffusion for small accumulated strains  $\dot{\gamma}\Delta t \simeq \Delta\gamma_{cage} \ll 1$ . While its nature remains unclear, it was shown that the typical strain  $\Delta\gamma_{cage}$  roughly corresponded to the affine deformation  $\delta/a$  at which particles come in direct contact (on average), which varies with volume fraction as  $(\phi_{rcp}/\phi)^{1/3} - 1$ , and vanishes as the average surface-surface separation between particles on approaching close packing.

In a very recent study by Wang *et al.* [109], the three-dimensional motion and diffusion of heavy tracer particles in an immersed, density matched granular packing ( $\phi \sim 0.6$ ) in a cylindrical Couette-cell was studied. Among many other remarkable results, the data in [109] showed direct evidence that  $D \propto \dot{\gamma}$  in non-Brownian systems. Interestingly, the value for shear diffusion in the vorticity direction,  $D/(\dot{\gamma}a^2) \simeq 0.1$  was close to the values found by Breedveld for slightly lower density.

Another study on non-Brownian suspensions [164] focussed on a transition from reversible to irreversible particle dynamics in oscillatory shear. While the creeping (Stokes) flow equations for simple shear flow are in principle reversible, particle roughness, three particle collisions or repulsive forces (ignoring Brownian motion) may render the dynamics irreversible. Pine *et al.* showed that there exists a volume-fraction-dependent critical strain amplitude beyond which the dynamics become diffusive. In a follow-up study [165], they demonstrated that the state below the critical strain is in fact an 'absorbing state', where the particles self-organize into a structure where collisions are avoided. They also demonstrated an increase in the dynamic viscosity of the suspension on crossing the critical strain amplitude, as was also observed previously by Breedveld *et al.* [140]. An interesting question is whether any relation exists between the absorbing states measured in these non-Brownian systems and the behaviour below the yield strain in colloidal glasses.

To date, flow studies of Brownian and non-Brownian systems have largely been conducted independently. It is clear that much can be gained by detailed comparison

of such studies [166] and that single-particle imaging can provide crucial insights in this exercise [129, 167].

## B. Ordered systems and ordering under flow

Hard spheres colloids undergo an entropy driven fluid-crystal phase transition when the suspension's volume fraction reaches  $\phi_f = 0.494$ . This behaviour was first confirmed experimentally using quasi-monodisperse hard-sphere-like PMMA colloids [6]. Static light scattering [168] shows (and later, conventional microscopy [81] confirms) that the resulting colloidal crystals consist of hexagonally-packed layers more or less randomly stacked on top of each other; i.e., these crystals have a mixture of face-centered cubic (fcc) and hexagonal close packed (hcp) structures. Starting with a paper in 1998 [169], van Meegen and co-workers have published a series of studies in the kinetics of crystallization in PMMA suspensions using time-resolved dynamic and static light scattering, investigating in particular the effect of polydispersity [170] in some detail.

Gasser and co-workers [84] pioneered the use of confocal microscopy to study the kinetics of colloidal crystallization. Using buoyancy-matched PMMA particles, they observed nucleation and growth of colloidal crystals with single-particle resolution. These authors identified the size of critical nuclei, 60-100 particles, in rough agreement with computer simulations [171], and to measure nucleation rates and the average surface tension of the crystal-liquid interface. For completeness we mention that Palberg and coworkers have pioneered the use of non-confocal microscopy methods to image ordering in highly-deionized suspensions [87, 172], which crystallise at very low volume fractions ( $10^{-3}$  or lower).

The relative mechanical weakness of colloidal crystal compared to their atomic and molecular counterparts means that modest shear will have large, non-linear effects on crystallisation as well as crystal structure. In the case of hard-sphere-like PMMA colloids, these effects have been studied using light scattering [173] since almost immediately after the discovery of crystallisation in this system [6]. Much more recently, confocal microscopy has been used to image shear effect in PMMA colloids. Below, we focus on reviewing such studies, but we note that imaging studies of crystallisation in other colloids have also been performed (see, e.g., [87]). To date, there have been few imaging studies of shear effects on ordering and ordered states in non-Brownian suspensions. We review briefly one series of such work at the end of this section.

### 1. Hard-sphere colloids

It is known from static light scattering [173], diffusing wave echo spectroscopy [86] and conventional optical microscopy [85] that the application of oscillatory



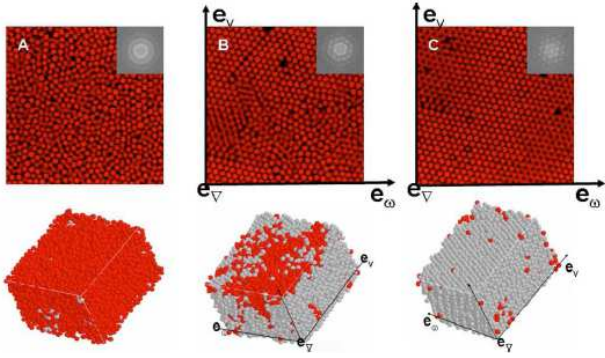


FIG. 13: Reprinted with permission from [94]. Copyright [2006], American Institute of Physics. Confocal images (top row, with insets showing the Fourier transform) and reconstructed 3D stacks (bottom row) showing the time dependent effect of oscillatory shear (frequency = 3 Hz, strain amplitude = 1) on a 48% volume fraction PMMA suspension. Time progresses from left to right: quiescent (24 hours after preparation, A), after 2 minutes (B), and after 5 minutes (C) of shear. In (B) and (C), unit vectors ( $\mathbf{e}$ ) in the the velocity ( $\mathbf{v}$ ), vorticity ( $\boldsymbol{\omega}$ ) and shear gradient ( $\nabla$ ) directions are shown. The light grey particles in the 3D renderings (bottom row) represent those with a high degree of local crystalline ordering.

shear to dense colloidal fluids or glasses can drive crystallisation. Rheological studies [174] show that shear-crystallised samples have lower elastic and viscous moduli than their glassy counterparts at the same volume fraction, in agreement with the enhanced effective ‘cage’ volume in the ordered case, leading to smaller entropic stiffness.

A detailed confocal imaging study of shear-induced crystallisation in hard-sphere colloids was performed recently by Solomon and Solomon [94]. They imaged crystals formed under an oscillatory shear field at a particle volume fraction of 52% in slightly-charged PMMA particles (diameter 1.15  $\mu\text{m}$ , polydispersity 4%) in a planar shear cell (Section II C 1). Particles were identified using the conventional Crocker and Grier algorithm but, due to the low acquisition rate (0.6 frames/second), imaging was only possible after the cessation of shear. Consistent with previous work [85, 173], they observed ordering of the initially amorphous suspension into close-packed planes parallel to the shearing surface, Figure 13. Upon increasing the amplitude of the applied oscillatory strain,  $\gamma$ , the close-packed direction of these planes was observed to shift from an orientation parallel to the vorticity direction to one parallel to the flow direction, and the quality of the layer ordering decreased. In addition, they studied shear-induced stacking faults and reported their three dimensional structure. For large STRAIN amplitudes ( $\gamma = 3$ ), ordering in the flow-vorticity plane only persisted for 5 to 10 layers, while in the gradient direction the crystal consists of alternating sequences of fcc and hcp layers.

Once formed, whether it be under quiescent or sheared

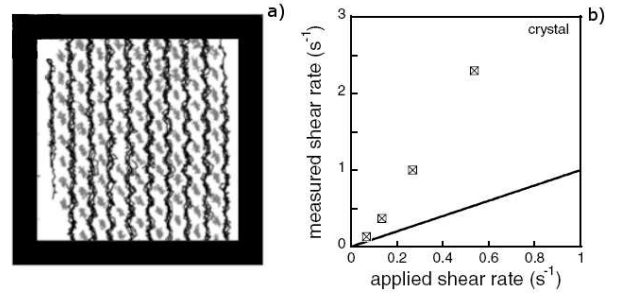


FIG. 14: Reprinted with permission from [111], copyright [2004], Institute of Physics Publishing (a) Superposition of particle tracks in the zero-velocity plane plus one adjacent plane in a sheared colloidal crystal, showing zig-zag motion. The image size is 18.75  $\mu\text{m} \times 18.75 \mu\text{m}$  (256  $\times$  256 pixels). The colloids have a diameter of 1.50  $\mu\text{m}$ . (b) Measured shear rate versus applied shear rate for the colloidal crystal (points), the continuous line shows equality of these two rates.

conditions, colloidal crystals show a complex response to applied stress. In particular, they exhibit banding under simple shear. We have already discussed flow localization in colloidal glasses in Section IV A 1. The first evidence for the occurrence of this phenomenon in ordered structures was reported in a study of hard-sphere colloidal crystals under steady shear by Derks *et al.* [111]. They studied the velocity profiles and single-particle dynamics via correlation techniques and particle tracking in a cone-plate system (Section II C 2) around the zero-velocity plane. Since particles were locked in their lattice positions and their motion was limited, they could be tracked using the conventional Crocker-Grier algorithm. The close-packed direction in hexagonally-ordered planes was observed to be parallel to the velocity, in agreement with high strain amplitude oscillatory shear results [85, 94]. The study also showed direct evidence that colloids in adjacent layers move in a zig-zag fashion, Figure 14(a), as previously inferred from light scattering [175] and conventional imaging [85]. The velocity profile measured over the accessible  $z$  range were linear, but the measured shear rates were much larger than the applied rates, Figure 14(b), indicating considerable shear banding in the sample. In a more recent study [176], Derks *et al.* analysed in more detail the particle dynamics in the flow-vorticity plane of a sheared crystal. They evidenced increasing fluctuations in the crystal layers on increasing rate, eventually leading to shear melting when the short-time mean square displacements due to shear attained a ‘Lindemann’ value of  $\sim 12\%$  of the particle separation.

More direct evidence of shear banding in colloidal crystals under *oscillatory* shear was found by Cohen and co-workers [102]. In this confocal microscopy study, the oscillatory motion across the gap was measured at various applied amplitudes and frequencies. For low applied deformation,  $\gamma_{\text{app}}$ , the authors claim that the crystal is linearly strained at all frequencies,  $f$ . At higher  $\gamma_{\text{app}}$ , the

crystal yields, and two different regimes are observed. At low frequencies, a high-shear band appears close to the upper (static) plate. As the applied strain and frequency increase, the band becomes larger until the whole gap is sheared at  $f > 3$  Hz. Moreover, large slip is observed in all cases, with the measured strain always below the applied one. Cohen *et al.* proposed a model based on the presence of two coexisting, linearly-responding phases to explain their observations. This model is attractive for its simplicity, but questions remain, in particular concerning the lack of bulk strain for small-amplitude, low-frequency data and some significant deviations between the modelled and measured profiles.

Simple shear is, of course, a highly idealised deformation geometry. Motivated partly by the possibility of shedding light on the deformation, fatigue and fracture of metals in more ‘real-life’ situations, Schall and co-workers carried out a confocal imaging study of a more complex form of deformation: indentation in defect-free colloidal crystals grown by slowly sedimenting silica particles on templated surfaces [177]. Indentation (or nano-indentation in the case of metallic crystals) consists in pressing a sharp tip (diamond for metals, and a needle for colloidal crystals) against a surface to probe its mechanical properties by relating the applied pressure and the measured penetration. It is also a method for the controlled introduction of defects into a crystal.

Schall *et al.* indented colloidal crystals using a needle with an almost hemispherical tip of diameter  $40\mu\text{m}$ , inducing a strain field in which the maximum shear strain lies well below the contact surface. The tip diameter, particle radius and crystal thickness in their experiments were chosen to be similar to parameters in typical metallic nano-indentation experiments. The authors discussed their observations using a model that addresses the role played by thermal fluctuations in the nucleation and growth of dislocations.

We have already discussed confinement effects in the channel flow of colloidal glasses. Such effects are also seen in hard-sphere colloidal crystals sheared between parallel plates. Cohen *et al.* [103] found that when the plate separation was smaller than 11 particle diameters, commensurability effects became dominant, with the emergence of new crystalline orderings. In particular, the colloids organise into “ $z$ -buckled” layers which show up in  $xy$  slices as one, two or three particle strips separated by fluid bands, Figure 15. By comparing osmotic pressure and viscous stresses in the different particle configurations, the cross-over from buckled to non-buckled states could be accurately predicted.

## 2. Non-Brownian suspensions

Shear induced structuring has been predicted in the flow of non-Brownian suspension (e.g. [178]), but to date there have been few imaging studies. In a series of experiments by Tsai and co-workers [108, 179, 180], laser

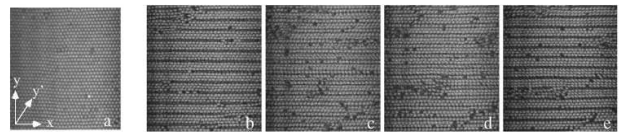


FIG. 15: Reprinted with permission from [103], copyright 2004 by the American Physical Society. Structure of a sheared suspension (diameter  $1.42\mu\text{m}$ ) with strain amplitude  $\gamma_0 = 0.38$ , frequency  $f = 30$  Hz and  $\phi = 0.61$ . The plate moves in the  $x$  direction. (a) Confocal micrograph of a sheared suspension forming hcp layers when the gap between the plates  $D = 80\mu\text{m}$ . (b)–(e) images of the suspension in the buckled state. The gap is set slightly below the height commensurate with confinement of four flat hcp layers. (b) an  $xy$  image slice of the suspension near the upper plate. (c)–(e) show slices that are, respectively, 1.3, 2.6, and  $3.9\mu\text{m}$  below the slice in (b).

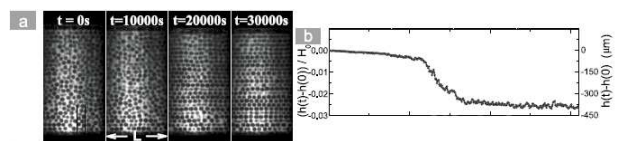


FIG. 16: Reprinted with permission from [108], copyright 2003 by the American Physical Society. (a) Time evolution of the structure of an index matched suspension of glass beads in [108], imaged in the flow-gradient plane after the start of shearing at  $t = 0$ . The observed layering is parallel to the flow direction. (b) Fractional volume compaction vs time, based on the change of height of the upper driving boundary. The actual change in microns is indicated at the right.

sheet imaging was employed to study the dynamics of confined glass sphere packings (diameter  $600\mu\text{m}$ ) in an index-matching (non-density matching) solvent in an annular shear cell with load applied from the top shearing surface. Using simultaneous measurements of the volume (and torque in [179]), they discovered a transition from a disordered packing to an ordered packing under steady shear, Figure 16(a), accompanied by compaction steps, Figure 16(b), and reduction of the shear force. They observed strongly non-linear shear profiles with a rapid reduction of the rate away from the top driving plate, varying significantly with the order of the packing. Due to these non-linear profiles, the delay observed before the ordering transition was strongly dependent on the layer thickness for fixed boundary speed, since global ordering requires an accumulated strain  $\Delta\gamma \sim 1$  through the entire sample.

## V. CONCLUSION AND OUTLOOK

Recent advances in imaging and data analysis techniques have enabled time resolved imaging and tracking of individual particles in colloidal systems under flow. We have reviewed these techniques, as well as examples of their application, primarily on concentrated systems

of hard-sphere colloids. Despite what has been achieved, we believe that this area is only in its infancy. Results already obtained raise many more questions than they answer. Many phenomena and systems remain little explored, and existing results invite further investigation using imaging techniques. For example, computer simulations of crystal nucleation [181] as well as proposed explanations of complex yielding behaviour in glassy states of systems of particles with short-range attraction [10, 11] can both be directly tested using such methods. In other cases, the use of imaging may throw light on well-known and long-studied phenomena that remain incompletely understood, e.g. shear thickening of concentrated colloidal suspensions [75]. The detailed comparative study of distinct but related systems using imaging techniques, e.g. Brownian and non-Brownian suspensions, or particulate suspensions and emulsions, should also be a fruitful area for exploration.

Further technical developments will enhance the power of the methodology. Faster scanning methods will obviously extend the upper limit of flow rates that can be studied. The development of algorithms for identifying [182] and tracking particles in polydisperse systems will significantly extend the range of systems that can be studied – there has been no quantitative study to date of polydisperse suspensions under flow by imaging. Further use of confocal imaging combined with (simultaneous) bulk rheometry will give a wealth of information on the relation between micro-scale dynamics and bulk flow and provide a crucial test ground for various theories. The coupling of three-dimensional imaging with mi-

cro-rheological techniques utilising optical trapping (‘laser tweezers’ [183]) should also yield many new discoveries and insights; confocal microscopy in two dimensions has already been used to explore the structure of the ‘wake’ downstream from a probe particle being dragged through a concentrated suspension [184]. Studying flow in microfluidic geometries using time-resolved single-particle imaging is of direct relevance to many emergent lab-on-a-chip type applications. And the parallel use of optical microscopy and other imaging techniques (perhaps especially NMR) to study the same flow system should open up many possibilities.

Finally, the example applications reviewed here pertain mostly to well-characterised, model particles. Confocal microscopy can fruitfully be used to image the (static) microstructure of many ‘real-life’ systems, such as foods [185]. To date, there have been few confocal microscopy and rheological studies of such systems [110]. Given the importance of rheological properties in the processing and utilisation of a wide range of industrial products (controlling the ‘mouth feel’ of food is but one example), we may expect increasing application of this methodology to applied colloidal systems.

## VI. ACKNOWLEDGEMENTS

RB, ABS and WCKP were funded respectively by EPSRC grants GR/S10377/01, EP/E030173/1 and EP/D067650. LI acknowledges support from EU network MRTN-CT-2003-504712.

- 
- [1] R. G. Larson, *The Structure and Rheology of Complex Fluids* (Oxford University Press, Oxford, 1999).
  - [2] J. Bent, L. R. Hutchings, R. W. Richards, T. Gough, R. Spares, P. D. Coates, I. Grillo, O. G. Harlen, D. J. Read, R. S. Graham, et al., *Science* **301**, 1691 (2003).
  - [3] M. E. Cates, *Annales Henri Poincaré Suppl.* **2**, S647 (2003).
  - [4] D. I. Wilson and S. L. Rough, *Chem. Engin. Sci.* **61**, 4147 (2006).
  - [5] F. Sciortino and P. Tartaglia, *Adv. Phys.* **54**, 471 (2005).
  - [6] P. N. Pusey and W. van Meegen, *Nature* **320**, 340 (1986).
  - [7] W. van Meegen, T. C. Mortensen, S. R. Williams, and J. Müller, *Phys. Rev. E* **58**, 6073 (1998).
  - [8] G. Petekidis, D. Vlassopoulos, and P. N. Pusey, *J. Phys.-Condens. Mat.* **16**, S3955 (2004).
  - [9] K. N. Pham, A. M. Puertas, J. Bergenholtz, S. U. Egelhaaf, A. Moussaid, P. N. Pusey, A. B. Schofield, M. E. Cates, M. Fuchs, and W. C. K. Poon, *Science* **296**, 104 (2002).
  - [10] K. N. Pham, G. Petekidis, D. Vlassopoulos, S. U. Egelhaaf, P. N. Pusey, and W. C. K. Poon, *Europhys. Lett.* **75**, 624 (2006).
  - [11] K. N. Pham, G. Petekidis, D. Vlassopoulos, S. U. Egelhaaf, W. C. K. Poon, and P. N. Pusey, *J. Rheol.* **52**, 649 (2008).
  - [12] J. T. Padding and A. A. Louis, *Phys. Rev. E* **74**, 031402 (2006).
  - [13] A. D. Dinsmore, E. R. Weeks, V. Prasad, A. C. Levitt, and D. A. Weitz, *Appl. Optics* **40**, 4152 (2001).
  - [14] P. Habdas and E. R. Weeks, *Curr. Opin. Colloid Interface Sci.* **7**, 196 (2002).
  - [15] D. Semwogerere and E. R. Weeks, in *Encyclopedia of Biomaterials and Biomedical Engineering* (Taylor and Francis, New York, 2005).
  - [16] V. Prasad, D. Semwogerere, and E. R. Weeks, *J. Phys.: Condens. Matter* **19**, 113102 (2007).
  - [17] W. W. Wood and J. D. Jacobson, *J. Chem. Phys.* **27**, 1207 (1957).
  - [18] W. G. Hoover and F. H. Ree, *J. Chem. Phys.* **49**, 3609 (1968).
  - [19] K. E. J. Barrett, *Dispersion Polymerization In Organic Media* (Wiley, London, 1975).
  - [20] L. Antl, J. W. Goodwin, R. D. Hill, R. H. Ottewill, S. M. Owens, S. Papworth, and J. A. Waters, *Colloid Surface.* **17**, 67 (1986).
  - [21] D. J. Cebula, J. W. Goodwin, R. H. Ottewill, G. Jenkin, and J. Tabony, *Colloid Polymer Sci.* **261**, 555 (1983).
  - [22] G. Bryant, S. R. Williams, L. Qian, I. K. Snook, E. Perez, and F. Pincet, *Phys. Rev. E* **66**, 060502 (2002).

- [23] A. S. Tse, Z. Wu, and S. A. Asher, *Macromol.* **28**, 6533 (1995).
- [24] R. Liu, M. A. Winnik, F. D. Stefano, and J. Vanketesan, *J. Polym. Sci. A – Polymer Chem.* **39**, 1495 (2001).
- [25] F. Tronc, M. Li, M. A. Winnik, B. L. Kaul, and J. C. Graciet, *J. Polymer Sci. A – Polymer Chem.* **41**, 766 (2003).
- [26] R. S. Jardine and P. Bartlett, *Colloids Surf. A* **211**, 127 (2002).
- [27] G. Bosma, C. Pathmamanoharan, E. H. A. de Hoog, W. K. Kegel, A. van Blaaderen, and H. N. W. Lekkerkerker, *J. Colloid Interf. Sci.* **245**, 292 (2002).
- [28] A. I. Campbell and P. Bartlett, *J. Colloid Interface Sci.* **256**, 325 (2002).
- [29] H. Hu and R. G. Larson, *Langmuir* **20**, 7436 (2004).
- [30] C. Pathmamanoharan, K. Groot, and J. K. G. Dhont, *Colloid Polymer Sci.* **275**, 897 (1997).
- [31] R. P. A. Dullens, E. M. Claesson, D. Derks, A. van Blaaderen, and W. K. Kegel, *Langmuir* **19**, 5963 (2003).
- [32] R. P. A. Dullens, E. M. Claesson, and W. K. Kegel, *Langmuir* **20**, 568 (2004).
- [33] R. P. A. Dullens, *Soft Matter* **2**, 805 (2006).
- [34] W. K. Kegel and A. van Blaaderen, *Science* **287**, 290 (2000).
- [35] S. M. Underwood and W. van Megen, *Colloid Polymer Sci.* **274**, 1072 (1996).
- [36] E. de Hoog, Ph.D. thesis, University of Utrecht (2001).
- [37] E. R. Weeks, J. C. Crocker, A. C. Levitt, A. Schofield, and D. A. Weitz, *Science* **287**, 627 (2000).
- [38] M. E. Leunissen, C. G. Christova, A. P. Hynninen, C. P. Royall, A. I. Campbell, A. I. M. Dijkstra, R. van Roij, and A. van Blaaderen, *Nature* **437**, 235 (2005).
- [39] A. Yethiraj and A. van Blaaderen, *Nature* **421**, 513 (2003).
- [40] H. Sedgwick, S. U. Egelhaff, and W. C. K. Poon, *J. Phys.: Condens. Mat.* **16**, S4913 (2004).
- [41] W. Stöber, A. Fink, and E. Bohn, *J. Colloid Interface Sci.* **26**, 62 (1968).
- [42] A. van Blaaderen and A. Vrij, *Langmuir* **8**, 2921 (1992).
- [43] R. Nyffenegger, C. Quellet, and J. Ricka, *J. Colloid Interface Sci.* **159**, 150 (1993).
- [44] N. A. M. Verhaegh and A. van Blaaderen, *Langmuir* **10**, 1427 (1994).
- [45] A. Imhof, Ph.D. thesis, University of Utrecht (1996).
- [46] A. K. van Helden, J. W. Jansen, and A. Vrij, *J. Colloid Interf. Sci.* **81**, 354 (1981).
- [47] C. Pathmamanoharan, *Colloids Surf.* **34**, 81 (1988).
- [48] C. Pathmamanoharan, *Colloids Surf.* **50**, 1 (1990).
- [49] A. van Blaaderen and A. Vrij, *J. Colloid Interface Sci.* **156**, 1 (1993).
- [50] A. Vrij, J. W. Jansen, J. K. G. Dhont, C. Pathmamanoharan, M. M. Kops-Werkhoven, and H. M. Fijnaut, *Faraday Discuss.* **76**, 19 (1983).
- [51] F. Hendriks and A. Aviram, *Rev. Sci. Inst.* **53**, 75 (1982).
- [52] C. J. Murphy, *Anal. Chem.* **74**, 520A (2002).
- [53] Q. Ma, C. Wang, and X. Su, *J. Nanosci. Nanotech.* **8**, 1138 (2008).
- [54] R. Brown, *The miscellaneous botanical works of Robert Brown* (R. Harwicke, London, 1866).
- [55] J. B. Perrin, *Les Atomes* (Alcan, Paris, 1913).
- [56] M. Raffel, C. Willert, and J. Kompenhans, *Particle Image Velocimetry, a Practical Guide* (Springer, Berlin, 1998).
- [57] W. Russel and M. Grant, *Colloid. Surface. A* **161**, 271 (2000).
- [58] R. Buscall, J. I. McGowan, and A. J. Morton-Jones, *Colloids Surf. A* **37**, 621 (1993).
- [59] P. D. Olmsted, *Rheol. Acta* **40**, 283 (2008).
- [60] S. P. Meeker, R. T. Bonnecaze, and M. Cloitre, *Phys. Rev. Lett.* **92**, 198302 (2004).
- [61] S. P. Meeker, R. T. Bonnecaze, and M. Cloitre, *J. Rheol.* **48**, 1295 (2004).
- [62] V. Breedveld, D. van den Ende, A. Tripathi, and A. Acrivos, *J. Fluid Mech.* **375**, 297 (1998).
- [63] V. Breedveld, D. van den Ende, M. Bosscher, R. J. J. Jongschaap, and J. Mellema, *Phys. Rev. E* **63**, 021403 (2001).
- [64] J.-B. Salmon, S. Manneville, A. Colin, and B. Pouligny, *Eur. Phys. J Appl. Phys.* **22**, 143 (2003).
- [65] S. Manneville, L. Bécu, and A. Colin, *Eur. Phys. J. Appl. Phys.* **28**, 361 (2004).
- [66] L. Bécu, S. Manneville, and A. Colin, *Phys. Rev. Lett.* **96**, 138302 (2006).
- [67] L. Bécu, D. Anache, S. Manneville, and A. Colin, *Phys. Rev. E* **76**, 011503 (2007).
- [68] E. Fukushima, *Ann. Rev. Fluid Mech.* **31**, 95 (1999).
- [69] P. T. Callaghan, *Rep. Prog. Phys.* **62**, 599 (1999).
- [70] D. Bonn, S. Rodts, M. Groenink, S. Rafai, N. Shahidzadeh-Bonn, and P. Coussot, *Ann. Rev. Fluid Mech.* **40**, 209 (2008).
- [71] L. F. Gladden and P. Alexander, *Meas. Sci. Technol.* **7**, 423 (1996).
- [72] G. Ovarlez, F. Bertrand, and S. Rodts, *J. Rheol.* **50**, 259 (2006).
- [73] J. S. Raynaud, P. Moucheront, J. C. Baudez, F. Bertrand, J. P. Guilbaud, and P. Coussot, *J. Rheol.* **46**, 709 (2002).
- [74] N. Huang, G. Ovarlez, F. Bertrand, S. Rodts, P. Coussot, and D. Bonn, *Phys. Rev. Lett.* **94**, 028301 (2005).
- [75] A. Fall, N. Huang, F. Bertrand, G. Ovarlez, and D. Bonn, *Phys. Rev. Lett.* **1**, 018301 (2008).
- [76] K. Zahn and G. Maret, *Phys. Rev. Lett.* **85**, 3656 (2000).
- [77] K. Zahn, A. Wille, G. Maret, S. Sengupta, and P. Nielaba, *Phys. Rev. Lett.* **90**, 155506 (2003).
- [78] F. Ebert, P. Keim, and G. Maret, *Eur. Phys. J. E* **26**, 161 (2008).
- [79] J. Baumgartl and C. Bechinger, *Europhys. Lett.* **71**, 487 (2005).
- [80] M. S. Elliot and W. C. K. Poon, *Adv. Colloid Interface Sci.* **92**, 133 (2001).
- [81] M. S. Elliot, B. T. F. Bristol, and W. C. K. Poon, *Physica A* **235**, 216 (1997).
- [82] T. Wilson, *Confocal Microscopy* (Academic Press, San Diego, 1990).
- [83] A. van Blaaderen and P. Wiltzius, *Science* **270**, 1177 (1995).
- [84] U. Gasser, E. R. Weeks, A. B. Schofield, P. N. Pusey, and D. A. Weitz, *Science* **292**, 258 (2001).
- [85] M. D. Haw, W. C. K. Poon, and P. N. Pusey, *Phys. Rev. E* **57**, 6859 (1998).
- [86] M. D. Haw, W. C. K. Poon, P. N. Pusey, P. Hebraud, and F. Lequeux, *Phys. Rev. E* **58**, 4673 (1998).
- [87] R. Biehl and T. Palberg, *Europhys. Lett.* **66**, 291 (2004).
- [88] P. Smith, G. Petekidis, S. U. Egelhaaf, and W. C. K. Poon, *Phys. Rev. E* **76**, 041402 (2007).
- [89] V. A. Tolpekin, M. H. G. Duits, D. van den Ende, and

- J. Mellema, *Langmuir* **20**, 2614 (2004).
- [90] H. Hoekstra, J. Vermant, and J. Mewis, *Langmuir* **21**, 9134 (2003).
- [91] E. J. Stancik, G. T. Gavranovic, M. J. O. Widenbrant, A. T. Laschtisch, J. Vermant, and G. G. Fuller, *Faraday Discuss.* **123**, 145 (2003).
- [92] P. Varadan and M. J. Solomon, *J. Rheol.* **47**, 943 (2003).
- [93] I. Cohen, T. G. Mason, and D. A. Weitz, *Phys. Rev. Lett.* **93**, 046001 (2004).
- [94] T. Solomon and M. J. Solomon, *J. Chem. Phys.* **124**, 134905 (2006).
- [95] E. Wang, C. M. Babbey, and K. W. Dunn, *J. Microscopy* **218**, 148 (2005).
- [96] R. Besseling, L. Isa, E. R. Weeks, and W. C. K. Poon, *Adv. Colloid Interface Sci.* **146**, 1 (2009).
- [97] P. Ballesta, R. Besseling, L. Isa, G. Petekidis, and W. C. K. Poon, *Phys. Rev. Lett.* **101**, 258301 (2008).
- [98] Y. L. Wu, J. H. J. Brand, J. L. A. van Gemert, J. Verkerk, H. Wisman, A. van Blaaderen, and A. Imhof, *Rev. Sci. Instrum.* **78**, 103902 (2007).
- [99] P. Hebraud, F. Lequeux, J. P. Munch, and D. J. Pine, *Phys. Rev. Lett.* **78**, 4657 (1990).
- [100] G. Petekidis, D. Vlassopoulos, and P. N. Pusey, *Faraday Discuss.* **123**, 287 (2003).
- [101] G. Petekidis, A. Moussaïd, and P. N. Pusey, *Phys. Rev. E* **66**, 051402 (2002).
- [102] I. Cohen, B. Davidovitch, A. B. Schofield, M. P. Brenner, and D. A. Weitz, *Phys. Rev. Lett.* **97**, 215502 (2006).
- [103] I. Cohen, T. G. Mason, and D. A. Weitz, *Phys. Rev. Lett.* **93**, 046001 (2004).
- [104] R. Besseling, E. R. Weeks, A. B. Schofield, and W. C. K. Poon, *Phys. Rev. Lett.* **99**, 028301 (2007).
- [105] J. F. Steffe, *Rheological methods in food processing engineering* (Freeman Press, East Lansing, MI, USA, 1996).
- [106] B. Rodriguez, M. Wolfe, and E. Kaler, *Langmuir* **9**, 12 (1993).
- [107] B. Aral and D. Kalyon, *J. Rheol.* **38**, 957 (1994).
- [108] J.-C. Tsai, G. A. Voth, and J. P. Gollub, *Phys. Rev. Lett.* **91**, 064301 (2003).
- [109] P. Wang, C. Song, C. Briscoe, and H. A. Makse, *Phys. Rev. E* **77**, 061309 (2008).
- [110] Y. Nicolas, M. Paques, D. van den Ende, J. K. G. Dhont, R. C. van Polanen, A. Knaebel, A. Steyer, J. P. Munch, T. B. J. Blijdenstein, and G. A. van Aken, *Food Hydrocolloids* **17**, 907 (2003).
- [111] D. Derks, H. Wisman, A. van Blaaderen, and A. Imhof, *J. Phys.: Cond. Mat.* **16**, S3917 (2004).
- [112] M. D. Haw, *Phys. Rev. Lett.* **92**, 185506 (2004).
- [113] L. Isa, R. Besseling, A. N. Morozov, and W. C. K. Poon, *Phys. Rev. Lett.* **102**, 058302 (2009).
- [114] J. R. Abbott et al., *J. Rheol.* **35**, 773 (1991).
- [115] D. Leighton and A. Acrivos, *J. Fluid Mech.* **181**, 415 (1987).
- [116] M. Frank, D. Anderson, E. R. Weeks, and J. F. Morris, *J. Fluid Mech.* **493**, 363 (2003).
- [117] D. Semwogerere, J. F. Morris, and E. R. Weeks, *J. Fluid Mech.* **581**, 437 (2007).
- [118] G. Degre, P. Joseph, P. Tabeling, S. Lerouge, M. Cloitre, and A. Ajdari, *Appl. Phys. Lett.* **89**, 024104 (2006).
- [119] A. C. J. Goyon, G. Ovarlez, A. Ajdari, and L. Bocquet, *Nature* **454**, 84 (2008).
- [120] C. J. Koh, P. Hookham, and L. G. Leal, *J. Fluid Mech.* **266**, 1 (1994).
- [121] A. Averbakh, A. Shauly, A. Nir, and R. Semiat, *Int. J. Multiphase Flow* **23**, 409 (1997).
- [122] A. Shauly, A. Averbakh, A. Nir, and R. Semiat, *Int. J. Multiphase Flow* **23**, 613 (1997).
- [123] M. K. Lyon and L. G. Leal, *J. Fluid Mech.* **363**, 25 (1998).
- [124] S. W. Sinton and A. W. Chow, *J. Rheol.* **35**, 735 (1991).
- [125] R. E. Hampton, A. A. Mammoli, A. L. Graham, N. Tetlow, and S. A. Altobelli, *J. Rheol.* **41**, 621 (1997).
- [126] D. Psaltis, S. R. Quake, and C. H. Y. CH, *Nature* **442**, 381 (2006).
- [127] J. C. Conrad and J. A. Lewis, *Langmuir* **24**, 7628 (2008).
- [128] L. Isa, R. Besseling, E. R. Weeks, and W. C. K. Poon, *J. Phys.—Conference Series* **40**, 124 (2006).
- [129] L. Isa, R. Besseling, and W. C. K. Poon, *Phys. Rev. Lett.* **98**, 198305 (2007).
- [130] J. N. Lee, C. Park, and G. M. Whitesides, *Anal. Chem.* **75**, 6544 (2003).
- [131] D. Bartolo, G. Degre, P. Nghe, and V. Studer, *Lab Chip* **8**, 274 (2008).
- [132] M. T. Roberts, A. Morhaz, K. T. Christensen, and J. A. Lewis, *Langmuir* **23**, 8726 (2007).
- [133] J. C. Crocker and D. G. Grier, *J. Colloid Interface Sci.* **179**, 298 (1996).
- [134] C. P. Brangwynne, G. H. Koenderink, E. Barry, Z. Dogic, F. C. MacKintosh, and D. A. Weitz, *Biophys. J.* **93**, 346 (2007).
- [135] M. Jenkins and S. U. Egelhaaf, *Adv. Colloid Interface Sci.* **136**, 65 (2008).
- [136] C. Beenhakker and P. Mazur, *Physica A* **126**, 249 (1984).
- [137] P. N. Pusey and R. J. A. Tough, *Farad. Discuss.* **76**, 123 (1983).
- [138] M. Tokuyama and I. Oppenheim, *Phys. Rev. E* **50**, R16 (1994).
- [139] J. Brady, *J. Chem. Phys.* **567**, 99 (1993).
- [140] V. Breedveld, D. van den Ende, R. J. J. Jongshaap, and J. Mellema, *J. Chem Phys.* **114**, 5923 (2001).
- [141] V. Breedveld, D. van den Ende, M. Bosscher, R. J. J. Jongshaap, and J. Mellema, *J. Chem Phys.* **116**, 10529 (2002).
- [142] H. Xu, A. P. Reeves, and M. Y. Louge, *Rev. Sci. Instrum.* **75**, 811 (2004).
- [143] G. Brambilla, D. E. Masri, M. Pierno, L. Berthier, L. Cipelletti, G. Petekidis, and A. B. Schofield, *Phys. Rev. Lett.* **102**, 085703 (2009).
- [144] R. Besseling, P. Ballesta, L. Isa, G. Petekidis, and W. C. K. Poon, in preparation.
- [145] P. R. ten Wolde, M. J. Ruiz-Montero, and D. Frenkel, *The Journal of Chemical Physics* **104**, 9932 (1996).
- [146] M. L. Falk and J. S. Langer, *Phys. Rev. E* **57**, 7192 (1998).
- [147] M. Fuchs and M. E. Cates, *J. Rheol.* (2009).
- [148] K. S. Schweizer and E. J. Saltzman, *J. Chem. Phys.* **119**, 1181 (2003).
- [149] E. J. Saltzman and K. S. Schweizer, *J. Chem. Phys.* **119**, 1197 (2003).
- [150] V. Kobelev and K. S. Schweizer, *Phys. Rev. E* **71**, 021401 (2005).
- [151] E. J. Saltzman, G. Yatsenko, and K. S. Schweizer, *J. Phys. Condens. Matter* **20**, 244129 (2008).
- [152] P. Schall, D. A. Weitz, and F. Spaepen, *Science* **318**, 1895 (2007).

- [153] J. S. Langer, *Scripta Materialia* **54**, 375 (2005).
- [154] U. Yilmazer, C. G. Gogos, and D. M. Kalyon, *Polymer Composites* **10**, 242 (1989).
- [155] D. M. Kalyon, *J. Rheol.* **49**, 621 (2005).
- [156] S. C. Jana, B. Kapoor, and A. Acrivos, *J. Rheol.* **39**, 1123 (1995).
- [157] M. Fuchs and M. E. Cates, *Phys. Rev. Lett.* **89**, 248304 (2002).
- [158] P. R. Nott and J. F. Brady, *Journal of Fluid Mechanics* **275**, 157 (1994).
- [159] C. S. Campbell, *Powder Tech.* **162**, 208 (2006).
- [160] G. D. R. MiDi, *Eur. Phys. J. E* **14**, 341 (2004).
- [161] R. R. Huilgol and Z. You, *J. Non-Newton. Fluid Mech.* **128**, 126 (2005).
- [162] O. Pouliquen and R. Gutfraind, *Phys. Rev. E* **53**, 552 (1996).
- [163] R. Gutfraind and O. Pouliquen, *Mech. Mater.* **24**, 273 (1996).
- [164] D. J. Pine, J. P. Gollub, J. F. Brady, and A. M. Leshansky, *Nature* **438**, 997 (2005).
- [165] L. Corte, P. M. Chaikin, J. P. Gollub, and D. J. Pine, *Nature Physics* **4**, 420 (2008).
- [166] P. Coussot and C. Ancey, *Phys. Rev. E* **59**, 4445 (1999).
- [167] L. Isa, R. Besseling, A. B. Schofield, and W. C. K. Poon (2008), in preparation.
- [168] P. N. Pusey, W. van Meegen, P. Bartlett, B. J. Ackerson, J. G. Rarity, and S. M. Underwood, *Phys. Rev. Lett.* **63**, 2753 (1989).
- [169] S. I. Henderson and W. van Meegen, *Phys. Rev. Lett.* **80**, 877 (1998).
- [170] H. J. Schope, G. Bryant, and W. van Meegen, *Phys. Rev. E* **74**, 060401 (2006).
- [171] S. Auer and D. Frenkel, *Nature* **409**, 1020 (2001).
- [172] R. Biehl and T. Palberg, *Rev. Sci. Instr.* **75**, 906 (2004).
- [173] B. J. Ackerson and P. N. Pusey, *Phys. Rev. Lett.* **61**, 1033 (1988).
- [174] N. Koumakis, A. B. Schofield, and G. Petekidis, *Soft Matter* **4**, 2008 (2008).
- [175] B. J. Ackerson, *J. Rheol.* **34**, 553 (1990).
- [176] x. A. v. B. Didi Derks, \* Yu Ling Wu and A. Imhof, *Soft Matter* **5**, 1060 (2009).
- [177] P. Schall, I. Cohen, D. A. Weitz, and F. Spaepen, *Nature* **440**, 319 (2006).
- [178] A. Sierou and J. F. Brady, *J. Rheol.* **46**, 1031 (2002).
- [179] J.-C. Tsai and J. P. Gollub, *Phys. Rev. E* **70**, 031303 (2004).
- [180] J.-C. Tsai and J. P. Gollub, *Phys. Rev. E* **72**, 051304 (2005).
- [181] R. Blaak, S. Auer, D. Frenkel, and H. Lowen, *Phys. Rev. Lett.* **93**, 068303 (2004).
- [182] R. Penfold, A. D. Watson, A. R. Mackie, and D. J. Hibberd, *Langmuir* **22**, 2005 (2006).
- [183] T. A. Waigh, *Rep. Prog. Phys.* **68**, 685 (2004).
- [184] A. Meyer, A. Marshall, B. G. Bush, and E. M. Furst, *J. Rheol.* **50**, 77 (2006).
- [185] N. Lorén, M. Langton, and A. M. Hermansson, in *Understanding and controlling the microstructure of complex foods* (CRC Press, Cambridge, 2007), pp. 232–260.